

RESEARCH ARTICLE

10.1029/2019JD030952

Key Points:

- Impacts of aerosol and thermodynamics conditions on deep convective systems are investigated using a bin microphysical model
- Increasing aerosol concentrations promote stronger convective precipitation in both the maritime and continental case
- Increasing aerosol concentrations increases graupel (hail) in maritime (continental) case owing to height of snow-dominant layer

Supporting Information:

- Supporting Information S1
- Figure S1
- Figure S2
- Figure S3
- Figure S4
- Figure S5
- Figure S6
- Figure S7
- Figure S8
- Table S1

Correspondence to:

T. Iguchi,
takamichi.iguchi@nasa.gov

Citation:

Iguchi, T., Rutledge, S. A., Tao, W.-K., Matsui, T., Dolan, B., Lang, S. E., & Barnum, J. (2020). Impacts of aerosol and environmental conditions on maritime and continental deep convective systems using a bin microphysical model. *Journal of Geophysical Research: Atmospheres*, 125, e2019JD030952. <https://doi.org/10.1029/2019JD030952>

Received 3 MAY 2019

Accepted 5 MAY 2020

©2020. American Geophysical Union.
All Rights Reserved.

This article has been contributed to by
US Government employees and their
work is in the public domain in the
USA.

Impacts of Aerosol and Environmental Conditions on Maritime and Continental Deep Convective Systems Using a Bin Microphysical Model

Takamichi Iguchi^{1,2} , Steven A. Rutledge³ , Wei-Kuo Tao² , Toshi Matsui^{1,2} ,
Brenda Dolan³ , Stephen E. Lang^{2,4}, and Julie Barnum^{3,5} 

¹Earth System Science Interdisciplinary Center, University of Maryland, College Park, MD, USA, ²NASA Goddard Space Flight Center, Greenbelt, MD, USA, ³Department of Atmospheric Science, Colorado State University, Fort Collins, CO, USA, ⁴Science Systems and Applications, Inc., Lanham, MD, USA, ⁵Now at Laboratory for Atmospheric and Space Physics, Boulder, CO, USA

Abstract A series of model simulations were conducted to investigate the effects of cloud condensation nuclei (CCN) loading and convective available potential energy (CAPE) on tropical maritime and midlatitude continental deep convection. Dynamical downscaling from global aerosol reanalysis was used to represent aerosol fields for the two convective regimes. We describe a control run and multiple sensitivity experiments using a limited-area model, employing spectral-bin cloud microphysics. The CCN loading is perturbed between the target maritime and continental conditions, roughly 40–2,000 cm⁻³ at 850 hPa and 1% supersaturation. Surface precipitation rates monotonically increase with increasing CCN loading for both the maritime and continental situations, while these monotonic increases are disrupted in the simulations with reduced CAPE. The increase in precipitation is in the form of convective precipitation, at the expense of stratiform precipitation. CCN increases promote increases in supercooled cloud water, in agreement with previous modeling studies. However, in the simulations investigated herein, the changes in supercooled water have different impacts on the cloud microphysics in the maritime and continental simulations. Increased supercooled water contents lead to more hail and less graupel in the continental simulation. For the maritime simulation, enhanced supercooled cloud water contents promote an increase in graupel since little or no hail is produced. This distinction is due to the difference in relative magnitudes and peak altitudes of supercooled water and snow amounts, which is further attributable to moisture and dynamical differences in the two cases.

1. Introduction

Thermodynamics (CAPE; convective available potential energy) and aerosol concentrations, specifically cloud condensation nuclei (CCN) are two distinct factors that impact the characteristic differences of midlatitude continental and tropical maritime convection (e.g., Rosenfeld & Lensky, 1998; Xu & Zipser, 2012; Matsui et al., 2016). The vertical distributions of temperature and moisture fundamentally impact atmospheric instability necessary for the development of convection. Vertical wind shear also exerts a strong control on convective structure (e.g., Rotunno et al., 1988; Weisman & Klemp, 1982, 1984). Although CAPE is sometimes similar between midlatitude continental and deep tropical maritime locales, the vertical distributions of thermal buoyancy are distinctly different, resulting in weaker updrafts and sharper reflectivity gradients in tropical convection versus midlatitude convection (Lucas et al., 1994a, 1994b; Xu & Randall, 2001; Zipser & Lutz, 1994). Another substantial factor is the distinct difference in the concentration of soluble aerosols between continental and maritime conditions, dictating first-order differences in cloud microphysical processes (e.g., Hudson & Yum, 2001; Squires, 1956, 1958; Squires & Twomey, 1960).

Sensitivity simulations with aerosol loading perturbations between typical maritime and continental conditions have been a subject of many previous studies (e.g., Jouan & Milbrandt, 2019; Loftus & Cotton, 2014; Noppel et al., 2010; Phillips et al., 2002). For example, Seifert and Beheng (2006; SB06, hereafter) provided a systematic modeling study regarding the evolution of convective systems under typical maritime and continental aerosol loadings, using a two-moment cloud microphysical scheme. They perturbed the initial CCN concentrations ranging from maritime (~100 cm⁻³) through continental (~1,000 cm⁻³). Parameters in a

power law function of supersaturation approximated observed CCN concentrations (e.g., Hegg et al., 1991), that is, $N_{CCN} = N_0 S^k$ (wherein N_{CCN} is the CCN concentration activated at supersaturation with respect to water S). The configuration based on the power law function for sensitivity experiments has been widely adopted in similar modeling studies with various cloud microphysical schemes to explore the responses of simulated convective clouds, not limited to typical maritime and continental differences in CCN but ranging from pristine to highly polluted conditions (e.g., Khain et al., 2004; Khain & Pokrovsky, 2004; Khain et al., 2008, 2009, 2010; Fan et al., 2009, Fan, Leung, et al., 2012; Fan, Rosenfeld, et al., 2012; Kalina et al., 2014, Lynn et al., 2005a, 2005b; , 2013; Seifert et al., 2006; Tao et al., 2007; Van den Heever et al., 2006; Wang, 2005). Some other studies altered the aerosol number concentration following size distribution functions (typically, unimodal or multimodal log-normal distribution) (e.g., Grabowski, 2011; Igel et al., 2013; Lee, 2017, Lebo & Morrison, 2014; Lebo & Seinfeld, 2011; Morrison & Thompson & Eidhammer, 2014; Saleeby et al., 2016). Yet other studies directly changed prescribed cloud droplet number concentration without explicit calculation of droplet nucleation from aerosol or CCN concentrations (e.g., Morrison, 2012; Rosenfeld, et al., 2008).

A possible key mechanism regarding the microphysical effect of aerosol particles on convective clouds with warm-cloud bases ($>0^\circ\text{C}$) is as follows: In condition with enriched hygroscopic aerosol particles, cloud droplet number concentration is high and cloud droplet size distribution is narrow as compared to that with fewer particles. Because smaller cloud droplets have reduced efficiency for coalescence, the formation of precipitation-sized drops is suppressed and so-called warm rain is delayed (e.g., Andreae et al., 2004; Rosenfeld & Lensky, 1998). When the convection is sufficiently deep to penetrate the 0°C isotherm, the impact on mixed-phase cloud microphysics is significant. Rosenfeld et al. (2008) proposed a conceptual model suggesting that more supercooled water as a result of the delayed warm-rain process caused more latent heat release via freezing, leading to invigoration of convection above the freezing level. On the other hand, changes in the duration and elevation of latent heat release were proposed as a mechanism for convective invigoration in studies using cloud-resolving simulations (e.g., Khain et al., 2005; 2015). Also, ultrafine CCN could be activated well above cloud base in some conditions, and the condensation growth of droplets from these CCN may lead to additional latent heat release (Khain et al., 2012; Khain & Pinsky, 2018). Recently, Fan et al. (2018) proposed the possibility of increase in condensation and associated latent heat release even for temperatures above 0°C when abundant ultrafine aerosol particles are ingested into deep convection.

Previous studies have discussed the microphysical impact of aerosol or CCN concentrations on cloud structure as well as precipitation. A central question among these studies is as follows: “Do increased CCN concentrations suppress or enhance precipitation, and what are their respective impacts on convective and stratiform precipitation?” The discussion has been reviewed and/or summarized by Rosenfeld et al. (2008), Levin and Cotton (2008), Khain et al. (2009), Khain and Lynn (2009), Lebo and Seinfeld (2011), and Tao et al. (2013), among others. Simulation-based studies in the literature have formed a consensus that both suppression and enhancement of precipitation occur, according to the type of cloud system simulated, the degree of the atmospheric instability, the structure of wind fields, etc. An important conclusion is that the sign and magnitude of the precipitation response varies depending on the numerical model specification and the specific experimental design. Observational studies are also conflicted as to the sign of the aerosol forcing in terms of increasing or decreasing precipitation. A well-known example of observed mechanism for precipitation suppression in maritime stratiform clouds is aerosol emission from ships, producing long-lived clouds marking the ship tracks (e.g., Albrecht, 1989; Radke et al., 1989). In contrast, the evidence of precipitation enhancement was extracted statistically from extensive sampling of satellite measurements for precipitation (e.g., Bell et al., 2008) and from long-term measurements for aerosol, cloud, precipitation, and other meteorological quantities at a field site (e.g., Li et al., 2011). However, several studies suspect the causality in the precipitation response to CCN changes, even though the correlation between precipitation and aerosol can be found in modeling or observational studies (e.g., Grabowski, 2015, 2018). The argument is based on the shortcomings of modeling studies, particularly sensitivity experiments with limited domains and short integration times for aerosol effects on deep convection, as well as limitations of meteorological observations. Grabowski (2018) showed that small changes in meteorological conditions that might be missed in the present observations could have similar or even larger impacts on convective systems than those due to changes in CCN loading from clean to polluted conditions.

This study organizes a series of model simulations for an intercomparison study of maritime and continental deep convective systems. Two case studies are undertaken, a midlatitude continental case and a tropical maritime case. Each case has a wealth of observations such as Doppler and polarimetric radars that provide important validation fields for the simulations. This study is just one of many studies on this topic, as discussed above. However, our study is unique in that we implement a method to provide and perturb requisite aerosol fields for numerical weather prediction (NWP) style cloud-resolving simulations. Simultaneously, vapor mixing ratio and consequently CAPE are perturbed in the simulations to investigate relative contributions of thermodynamics and aerosols on the deep convective systems as a follow-up of previous modeling (e.g., SB06, Storer et al., 2010; Grant & van den Heever, 2015) and observational (e.g., Stolz et al., 2015, 2017) studies.

In the series of aerosol sensitivity experiments we perform, three intermediate conditions are additionally configured between specific maritime and continental aerosol conditions. These experiments allow us to examine CCN impacts over a range of concentrations, rather than just two extremes (i.e., maritime vs. continental). Indeed, previous numerical studies (e.g., Fan et al., 2007; Jeon et al., 2018; Khain et al., 2011; Li et al., 2008; Wang, 2005) reported a nonmonotonic response to CCN concentrations and one goal of this study is to examine this further.

Descriptions of numerical experiments including overviews of the convective systems, model configurations, and experimental designs are presented in section 2. The simulation results are discussed in sections 3 and 4. Finally, summary and conclusions are provided in section 5.

2. Descriptions of Numerical Experiments

2.1. Synopses of Convective Systems for Simulations

One tropical maritime and one midlatitude continental deep convective cases have been selected from the Tropical Warm Pool International Cloud Experiment (TWP-ICE; May et al., 2008) and the Midlatitude Continental Convective Clouds Experiment (MC3E; Jensen et al., 2016) for model simulations, respectively.

2.1.1. The 23 January 2006 in TWP-ICE

TWP-ICE was conducted around Darwin, Northern Australia in January and February 2006. The deep convective system observed on 23 January 2006 was one of several mesoscale-convective systems (MCS) over the course of several days that produced significant rainfall (e.g., Boyle & Klein, 2010). The particular MCS was triggered by the passage of a low-pressure system from the east during an active monsoon period. Figure 6 of May et al. (2008) shows that the multicell convective system was widespread around the Darwin site on 23 January. Several previous studies have conducted model intercomparisons using cloud resolving models (CRMs) and/or limited-area models (LAMs) for this MCS case (e.g., Fridlind et al., 2012; Mrowiec et al., 2012; Petch et al., 2014; Varble et al., 2011; Varble et al., 2014a, 2014b; Zhu et al., 2012). These model intercomparison studies are reviewed by Krueger et al. (2016).

Figure 1a is a skew-T log-p plot of an atmospheric column sampled from the initial atmospheric condition (00 UTC 23 January 2006) of the Weather Research and Forecasting (WRF) model simulation, whose experimental design is described in section 2.4.1. The location of this atmospheric column is near the point with the highest CAPE in the simulation domain. The skew-T log-p plot depicts a low level of free convection (LFC; the bottom of the red dotted line) and very high equilibrium level (EL; the top of the red dotted line). The difference between the air temperature (black line) and the air-parcel temperature (red dotted line) is nearly constant throughout the column. The atmospheric column is partially saturated from ~1,000 to 500 hPa.

2.1.2. The 23–24 May 2011 in MC3E

MC3E took place from 22 April to 6 June 2011 around the Department of Energy (DOE) Atmospheric Radiation Measurement (ARM) South Great Plains (SGP) central facility in Oklahoma, under joint support from DOE and the National Aeronautics and Space Administration (NASA). The deep convective system observed on 23 May 2011 was one of three major convective events highlighted in Jensen et al. (2016). Pu and Lin (2015) provided a short description about the evolution of the system and summarized here. Isolated convection initiated along a strong dry line over western Oklahoma (Figure 10 of Jensen et al., 2016). Over the next few hours from 2100 UTC 23 May, these cells developed into a large multicell MCS over the SGP. The mature stage of the system lasted for a few hours (0000–0400 UTC 24

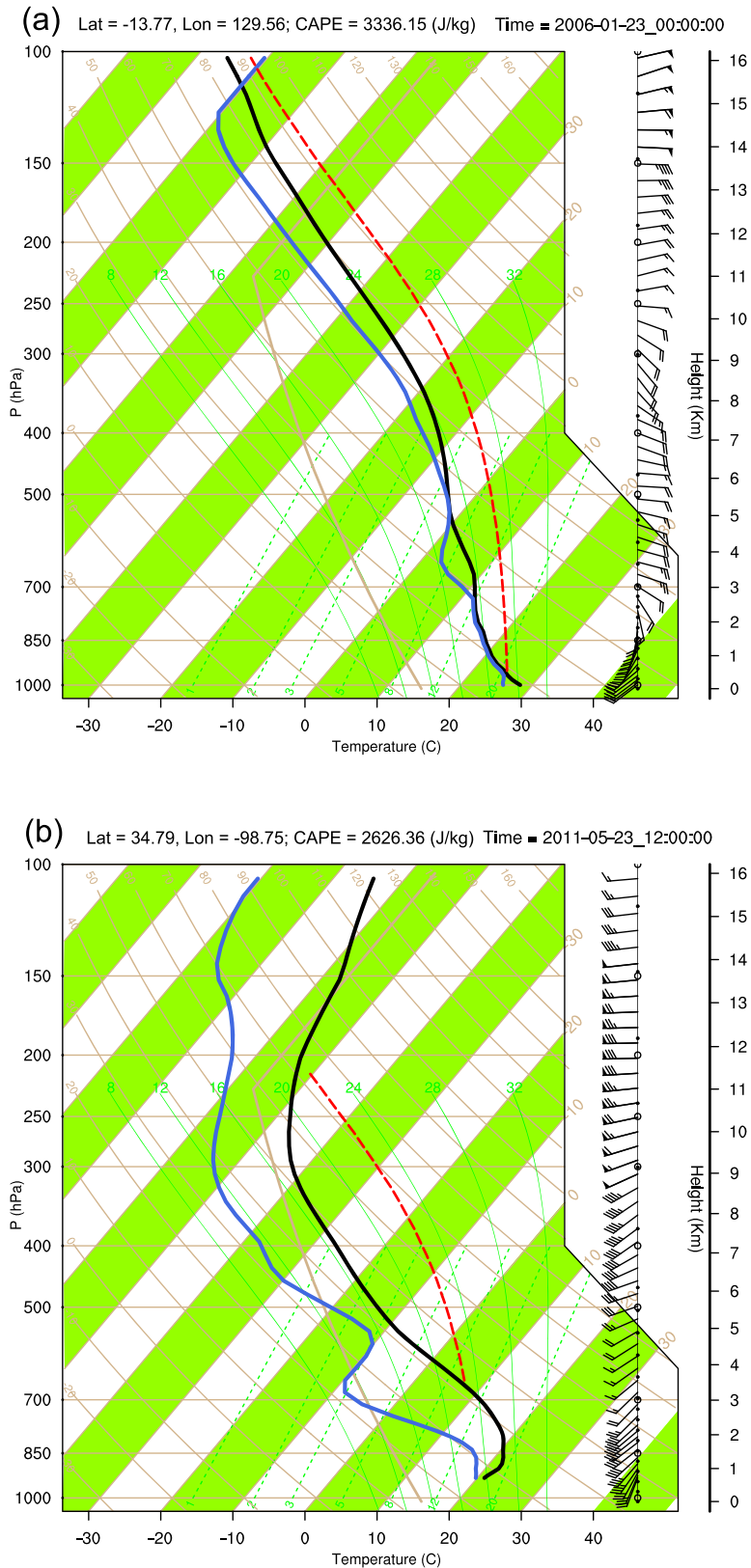


Figure 1. Skew-T log-p diagram of an atmospheric column near the horizontal grid point with the maximum CAPE in the initial condition field of the WRF model simulations for (a) the TWP-ICE case (00 UTC 23 January 2006) and (b) the MC3E case (12 UTC 23 May 2011).

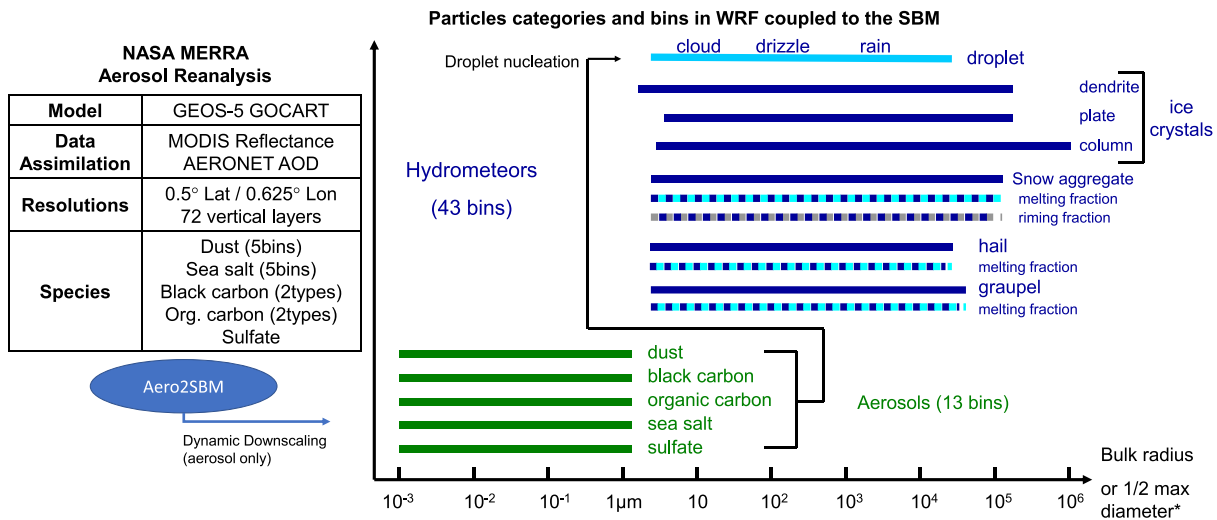


Figure 2. Conceptual diagram of the coupling between the NASA MERRA aerosol reanalysis (MERRAero) and WRF coupled to the SBM through dynamic aerosol downscaling. *The horizontal axis denotes half of the maximum diameter for ice crystals and the bulk radius of the others.

May), and the system slowly moved eastward as it dissipated. This convective complex has also been the subject of previous modeling studies (e.g., Fan et al., 2015; Marinescu et al., 2016; Pu & Lin, 2015; Saleeby et al., 2016; Tao et al., 2013).

Figure 1b shows a skew-T log-p plot sampled from the initial condition (12 UTC 23 May 2011) of the WRF model simulation for this MC3E case. Compared to that of the TWP-ICE case (Figure 1a), the atmospheric structure of this case is drier throughout the column and is characterized by a higher LFC and a lower EL. Although the CAPE is smaller than the TWP-ICE case, there is more instability over a shallower layer. In addition to these factors, the cold and dry air mass in the middle troposphere is suitable to the development of continental severe storms.

2.2. The WRF Model and the Spectral-Bin Microphysics Scheme

The version 3.6.1 of WRF Advanced Research configuration (WRF-ARW; Skamarock et al., 2008) is employed in this study. The SBM scheme of the Hebrew University Cloud Model (HUCM; e.g., Khain et al., 2011) was implemented into WRF-ARW 3.6.1 through our own coding work (Iguchi et al., 2012, 2014). The specification of the SBM scheme is slightly different from two SBM schemes in WRF-ARW (so-called Fast-SBM, e.g., Khain et al., 2010, and Full-SBM, e.g., Khain et al., 2004) which are also from HUCM.

In the SBM used herein, 43 bins with incremental particle masses are used to explicitly calculate the evolution of particle-size distribution (PSD) of each cloud particle type without assuming bulk size distribution functions. Cloud particle types are categorized into the following seven classes: water droplets (ranging from small cloud droplet to large raindrop sizes), three types of ice crystals (plate, column, and dendrite), snow aggregates, graupel, and hail (Figure 2). The change of PSD of each type is calculated considering advection and gravitational sedimentation as well as various cloud microphysical processes. Details of the parameterizations used to calculate the microphysics conversion terms can be found in, for example, Khain et al. (2011), Iguchi et al. (2012), and Iguchi et al. (2014).

Additional sets of 43 bins to explicitly compute the rimed mass portion of snow aggregates and the liquid mass portion of melting ice particles (snow, graupel, and hail) are also included in prognostic variables of the SBM scheme (Figure 2). These additional variables enable smooth transitions between specific cloud particle types by representing these intermediates states owing to riming and melting. Previous studies (Iguchi et al., 2012; Iguchi et al., 2014) showed that these functions for riming and melting were useful in investigating rimed snow in a lake effect snowstorm and bright band structure in mixed-phased precipitation.

Snow particles with bulk radii less than $\sim 550 \mu\text{m}$ are transformed to hail when the rimed mass fraction is over 95%; the rimed fraction of snow increases when smaller supercooled droplets are accreted by the snow. Snow particles over $550 \mu\text{m}$ bulk radius transition to graupel when their bulk densities are larger than 0.2 g cm^{-3} . The bulk density of a snow particle with rimed parts is calculated as a mass-weighted mean of the bulk densities of rimed parts with 0.9 g cm^{-3} and of dry snow parts with density prescribed according to the mass (shown, e.g., in Figure 1 of Iguchi et al., 2012). Graupel particles change to hail if their diameters are over 10 mm or if wet growth begins at subfreezing temperatures (Khain et al., 2011). The change of graupel to hail through the wet growth process occurs under condition with enriched supercooled water. Details of this wet growth parameterization can be found in the appendix of Khain et al. (2011). A threshold diameter of graupel for wet growth initiation (Dennis & Musil, 1973) is determined according to a heat balance condition on the wet graupel. Graupel particles of diameters larger than the threshold are transferred to hail.

Several recent updates of HUCM have not been implemented in the SBM used in this study yet. For example, time-dependent process of raindrop freezing and wet growth of hail/graupel (Iltoviz et al., 2016, 2018; Phillips et al., 2014, 2015) are not included. In the SBM we used, freezing of droplets with bulk radii less than $\sim 250 \mu\text{m}$ leads to the formation of plate-type ice crystals, while those over the bulk radius are transformed to hail particles immediately.

The ice-melting parameterization is basically identical to that in Phillips et al. (2007). Liquid water fractions of snow, graupel, and hail are explicitly predicted, while those of ice crystals are excluded and these crystals melt instantaneously. The theoretical model and equations for the melting of snow are based on those in Mitra et al. (1990) and are used to describe the thermodynamics and the conservation of mass among the three phases of water. The corresponding model and equations in Rasmussen and Heymsfield (1987) are used to calculate the melting processes of graupel and hail with water shedding.

2.3. Dynamical Downscaling of Aerosol Concentration From MERRA Global Aerosol Reanalysis to WRF With SBM

Dynamical downscaling of aerosol variables from the NASA Modern Era Retrospective analysis for Research and Applications Aerosol Reanalysis (MERRAero; da Silva et al., 2015) to WRF coupled with SBM (WRF-SBM, hereafter) has been implemented in this study. This downscaling approach from global-/large-scale aerosol (and chemical) transport model simulations to LAM cloud-resolving simulations is based on those in Iguchi et al. (2008) and Choi et al. (2014). The scientific background and merits of this approach are reviewed in Iguchi et al. (2015). Similar approaches have been proposed and developed for aerosol-cloud interaction study using bulk cloud microphysics (e.g., Li et al., 2009) and also bin microphysics (e.g., Gao et al., 2016). This approach provides spatial and temporal variability in the aerosol compositions into LAM simulations through downscaling. Although more realistic aerosol compositions and CCN concentrations can be obtained from in-situ measurements, they have limitations in the sampling for space and time and hence cannot address the spatial and temporal variability throughout a simulation domain and period.

MERRAero is produced by the Goddard Earth Observing System version 5 (GEOS-5; e.g., Molod et al., 2015) Atmospheric Global Climate Model coupled to the Goddard Chemistry, Aerosol, Radiation, and Transport (GOCART; Chin, Rood, et al., 2000; Chin, Savoie, et al., 2000) aerosol module. MERRAero contains 15 types of aerosol, that is, dust (five noninteracting size bins), sea salt (five noninteracting size bins), black and organic carbon (each type has both hydrophobic and hydrophilic components; thus four in total), and sulfate in the form of an externally-mixed aerosol mass mixing ratio (e.g., Randles et al., 2017). MERRAero has a horizontal grid spacing of 0.5° latitude by 0.625° longitude with 72 hybrid sigma-pressure vertical layers up to 0.01 hPa at 3-hourly intervals. It includes assimilated composites of cloud-clear reflectances derived from the Moderate Resolution Imaging Spectroradiometer (MODIS) sensor on both the Terra and Aqua satellites and calibrated aerosol optical depth (AOD) obtained from Aerosol Robotic Network (AERONET) observations.

The module to process downscaling from MERRAero to WRF-SBM (hereafter, Aero2SBM) is based on an implementation of WRF coupled to chemistry (WRF-Chem) in NU-WRF (e.g., Peters-Lidard et al., 2015). It adds aerosol variables to WRF initial and lateral boundary conditions through a process of an offline one-way nesting.

Table 1
Configurations of Sensitivity Simulations for the TWP-ICE and MC3E Cases

Abbreviation	Case	CCN conc. (cm^{-3}) at 850 hPa ^a	Vapor
TC1	TWP-ICE	39.3	100%
TC2	TWP-ICE	85.3	100%
TC3	TWP-ICE	215.0	100%
TC4	TWP-ICE	618.9	100%
TC5	TWP-ICE	1963.7	100%
TD1	TWP-ICE	39.3	95%
TD2	TWP-ICE	85.3	95%
TD3	TWP-ICE	215.0	95%
TD4	TWP-ICE	618.9	95%
TD5	TWP-ICE	1963.7	95%
MC1	MC3E	47.8	100%
MC2	MC3E	88.0	100%
MC3	MC3E	239.7	100%
MC4	MC3E	660.7	100%
MC5	MC3E	2000.7	100%
MD1	MC3E	47.8	80%
MD2	MC3E	88.0	80%
MD3	MC3E	239.7	80%
MD4	MC3E	660.7	80%
MD5	MC3E	2000.7	80%

^aRepresentative CCN concentrations of several other pressure levels are shown in Tables 2 and 3 also.

In Aero2SBM, a gridded field of the mass mixing ratio for each aerosol variable in MERRAero is regridded to match that of WRF for the initial and lateral boundary conditions. Then, the aerosol mass mixing ratios are converted to bulk number concentration (integrated over all particle sizes) of dry particles for the five aerosol types. The bulk number concentration for each aerosol type is further converted into a series of discrete number concentrations in 13 particle-size bins using assumed trimodal size distributions described in Choi et al. (2014). WRF-SBM predicts concentrations of the 13 size bins of the 5 aerosol types (65 in total), dynamically downscaled from MERRAero (Figure 2). The trimodal size distributions are different from the log-normal size distributions used in the GEOS-5 GOCART model (Chin et al., 2002; P. Colarco, personal communication 2017) to calculate aerosol optical thickness in the global aerosol transport simulations. The use of the different size distributions is based on better reproduction of CCN number concentrations in the comparison to observations at the ARM SGP central facility, described in section 3.1.1. (only the result using the trimodal size distributions is shown in this study).

The treatment of these aerosols in WRF-SBM is almost the same as in HUCM as well as Fast-SBM and Full-SBM in WRF-ARW: Heterogeneous nucleation of cloud droplets is initiated by aerosol particles in a supersaturated environment. A critical particle radius for each aerosol type in a supersaturated environment is determined on the basis of the Köhler curve theory (Köhler, 1936). Different hygroscopicity parameters for the five aerosol types (Table 1 in Ghan et al., 2001) are assumed to calculate the critical particle radius. The critical radius is calculated separately for the size distribution of each aerosol type. All aerosol particles larger than the critical radius for each aerosol type are allowed to nucleate, and then they are added up to the droplet size distribution.

Currently, heterogeneous nucleation of ice particles and heterogeneous freezing of droplets are parameterized independently of the predicted aerosol concentrations in the SBM. Also, aerosol concentrations have no impact on atmospheric radiation processes, and chemical and aerosol microphysical processes do not affect the aerosol concentration. No emission of aerosol particles from sea or land surfaces is considered, nor is their regeneration from completely evaporated or sublimated cloud particles. Hydrometeor particle size distributions calculated in the SBM are not linked to those in WRF atmospheric radiation schemes. For example, in the Goddard shortwave and longwave radiation schemes (Chou et al., 2001; Chou & Suarez, 1999), a fixed cloud droplet radius of 10 μm and ice effective radius that is a function of the air temperature are assumed. In summary, the present specification of aerosol particles in the SBM is limited to focusing on the impact of CCN, and it is suitable only for limited-area and short-period case studies.

Currently, heterogeneous nucleation of ice particles and heterogeneous freezing of droplets are parameterized independently of the predicted aerosol concentrations in the SBM. Also, aerosol concentrations have no impact on atmospheric radiation processes, and chemical and aerosol microphysical processes do not affect the aerosol concentration. No emission of aerosol particles from sea or land surfaces is considered, nor is their regeneration from completely evaporated or sublimated cloud particles. Hydrometeor particle size distributions calculated in the SBM are not linked to those in WRF atmospheric radiation schemes. For example, in the Goddard shortwave and longwave radiation schemes (Chou et al., 2001; Chou & Suarez, 1999), a fixed cloud droplet radius of 10 μm and ice effective radius that is a function of the air temperature are assumed. In summary, the present specification of aerosol particles in the SBM is limited to focusing on the impact of CCN, and it is suitable only for limited-area and short-period case studies.

2.4. Experiment Design of Simulations Using WRF-SBM

2.4.1. Base Configuration

Figure 3 illustrates geographical coverages of the WRF simulations for the TWP-ICE 23 January 2006 and MC3E 23–24 May 2011 cases. A simulation domain for each case is characterized by three nested domains. The three nested domains for the TWP-ICE case comprise 300×300 , 286×286 , and 334×334 grid points with horizontal grid intervals of 9, 3, and 1 km, respectively. The three nested domains for the MC3E case have 513×389 , 496×424 , and 673×595 grid points with the same set of horizontal grid intervals. The vertical columns extending through a top pressure of 50 hPa are divided into 60 layers with sigma-coordinate intervals increasing with altitude for the terrain-following bottom. In both TWP-ICE and MC3E cases, the innermost domains were subject to a series of sensitivity simulations using WRF-SBM. Prior to the sensitivity simulations, preliminary WRF simulations were conducted to calculate the lateral boundary meteorological conditions of the innermost domains.

The preliminary WRF simulation for the TWP-ICE case calculated the evolution of the atmospheric fields of the three nested domains simultaneously through two-way interactive grid nesting, from 00 UTC 21 January

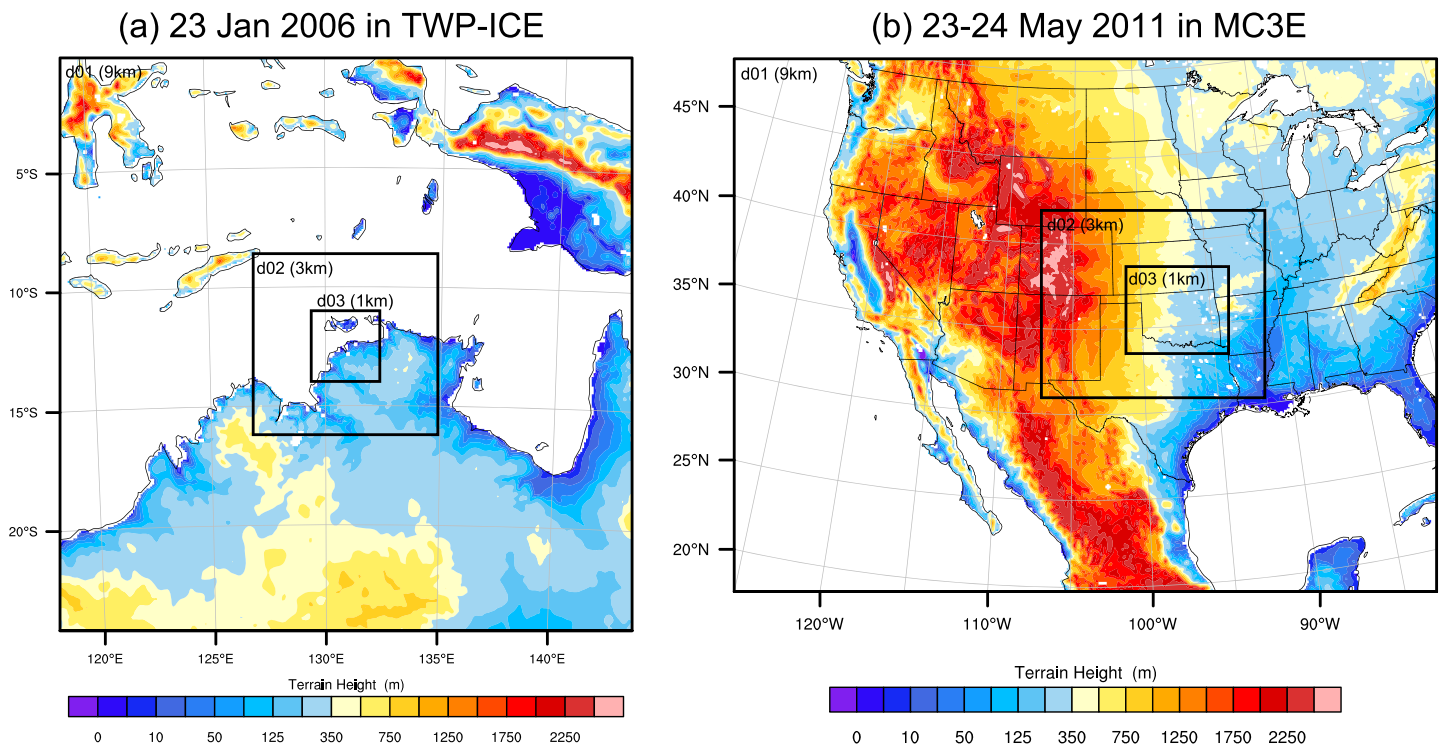


Figure 3. Domain configuration of the WRF simulations for (a) the TWP-ICE case and (b) the MC3E case.

through 00 UTC 26 January 2006. The initial meteorological condition of all the three domains and the lateral boundary condition of the outermost domain were calculated from the interim reanalysis of the European Centre for Medium-Range Weather Forecasts (ECMWF) model (ERA-Interim; Dee, 2011) with a spectral T255 horizontal resolution with 6-hourly intervals. The following physics parameterizations were used in this preliminary WRF simulation: the Goddard Cumulus Ensemble (GCE) single-moment four-ice bulk microphysics (Lang et al., 2014; Tao et al., 2016) for grid-scale cloud microphysics, the Grell-Freitas ensemble scheme (Grell & Freitas, 2014) as subgrid convection parameterization only in the domain with 9-km grid intervals, the Goddard shortwave and longwave radiation schemes (Chou et al., 2001; Chou & Suarez, 1999) for radiative flux and heating, the Mellor-Yamada-Janjic scheme (Janjic, 1994) for the planetary boundary layer and subgrid-scale turbulence calculation, the unified community Noah land surface model (Tewari, 2004) for the land surface processes and surface heat fluxes. Note that dynamic aerosol downscaling from MERRAero was not applied to this preliminary WRF simulation.

We tested three different global reanalysis, ERA-Interim, the National Center for Environmental Prediction (NCEP) Final (FNL) operational global analysis data set (NOAA/NCEP, 2000), and the NASA Modern-Era Retrospective analysis for Research and Applications, Version 2 (MERRA-2; Bosilovich et al., 2015) to drive the maritime simulation. In addition, the Morrison 2-moment cloud microphysics scheme (Morrison et al., 2009) in place of the GCE four-ice bulk microphysics was tested with ERA-Interim. Figure S1 (a supporting information) shows time series of hourly rainfall amounts from 00 UTC 21 through 00 UTC 26 January over the innermost domain (Figure 3a), which is comparable to time series of observed rainfall estimates in Boyle and Klein (2010); their Figure 2a). Within this set of four simulations, only the one using ERA-Interim with the GCE 4-ice bulk microphysics shows very high rainfall amounts (late on 23 January) that are consistent with the observation estimates. The difference in the simulations with the various data sets is depicted in animations for time series of surface rainfall over each simulation domain (Movie S1 in the supporting information). The animations show that the strong convective complex causing the very high rainfall amounts on 23 January over the innermost domain is an extension of a very large scale maritime storm system across the outermost domain (Figure 3a). The counterclockwise-rotating strong

Table 2
CCN Number Concentrations at 1% Supersaturation (cm^{-3}) at Specific Pressure Levels Calculated From the Initial Conditions of the Aerosol Sensitivity Simulations for the TWP-ICE Case (Table 1)

Pressure level (hPa)	TC1	TC2	TC3	TC4	TC5
	TD1	TD2	TD3	TD4	TD5
925	77.2	123.4	229.4	493.1	1187.5
850	39.3	85.3	215.0	618.9	1963.7
700	3.5	10.7	36.7	141.8	610.2
500	2.7	6.7	17.6	49.4	148.9

Note. The values are horizontally averaged over the innermost WRF domain for the TWP-ICE case (Figure 3).

convective complex moves to the southwest across the second domain. The position and timing of the development of the strong convective complex as well as its spatial pattern are quite sensitive to the selection of the reanalysis data sets used to drive the simulation.

Three-hourly outputs of the intermediate domain with grid spacings of 3 km in the preliminary simulation were used to establish the lateral boundary condition of the WRF-SBM simulations for the innermost domain only through an offline one-way nesting. The same physical parameterizations as in the preliminary simulation were adopted, except for the grid-scale cloud microphysics scheme. Mass mixing ratios of hydrometeors output from the GCE 4-ice bulk microphysics in the preliminary simulation were excluded from the lateral boundary condition such that its output did not directly affect the simulated cloud fields of the innermost domain with the SBM. Aero2SBM added the 65 aerosol variables

into the initial and lateral boundary conditions. Then, WRF-SBM simulated the atmospheric fields from 00 UTC 23 January through 00 UTC 24 January (24 hr).

The simulations for the MC3E case were conducted on the basis of almost the same two-step process as in the TWP-ICE case. Both preliminary and WRF-SBM simulations were integrated from 12 UTC 23 May through 12 UTC 24 May 2011. NCEP FNL was used for the initial and lateral boundary conditions in the MC3E case, selected on the basis of intercomparison of the simulations with the three global reanalysis data sets, similar to the TWP-ICE case.

Table 1 lists sensitivity experiments using WRF-SBM for the innermost simulation domains. Each TWP-ICE or MC3E case has a set of 10 simulations including the baseline simulations (TC1 and MC5) and those with perturbed aerosol and/or thermodynamics conditions given in the subsections below.

2.4.2. Aerosol Perturbation

The initial and lateral boundary conditions of the aerosol concentrations in WRF-SBM are determined using the downscaling from MERRAero described in section 2.3. The baseline simulations (TC1 and MC5) use aerosol fields derived from the times and domains corresponding to the TWP-ICE or MC3E case. Four additional aerosol conditions are prepared to form a series of sensitivity experiments for both the TWP-ICE and MC3E cases (Table 1). The range of aerosol concentrations spans the range of CCN loadings between the (low) tropical maritime TWP-ICE and the (high) continental midlatitude MC3E case.

The aerosol concentrations are perturbed while preserving the patterns in the spatial and temporal distribution downscaled from MERRAero in the series of sensitivity simulations. The distribution of aerosol concentration may be correlated with the meteorological fields as well as the distribution of land surface types. Implementation of realistically inhomogeneous aerosol fields results in better simulations of the distribution of cloud microphysical properties (e.g., Iguchi et al., 2008).

Tables 2 and 3 show CCN number concentrations at 1% supersaturation at several pressure levels (regridded from the WRF sigma-vertical coordinate) calculated from horizontally-averaging the initial conditions of the aerosol sensitivity simulations shown in Table 1. The concentrations at 925 hPa levels in the simulations of both ends are similar to some of representative values observed from maritime and continental air masses shown in Pruppacher and Klett (1997). The three additional conditions correspond roughly to quarterly intermediates on a logarithmic scale between these both ends.

2.4.3. Thermodynamics Perturbation

The method to perturb the thermodynamic condition is basically based on that in Weisman and Klemp (1982) as well as SB06. Thermodynamic fields are perturbed by altering water vapor mixing ratios. In subsets of the sensitivity experiments (Table 1), the water vapor mixing ratios are homogeneously reduced to 95% of the original values in the TWP-ICE case and to 80% of the original values in the MC3E case for both initial and lateral boundary conditions. As a result, CAPE values representing the domain average in the WRF domain get roughly a 15% reduction in the original CAPE values for both cases. Figure 4 shows time series of

Table 3
Same as Table 2 but for the MC3E Simulations

Pressure level (hPa)	MC1	MC2	MC3	MC4	MC5
	MD1	MD2	MD3	MD4	MD5
925	159.8	235.8	391.8	716.2	1398.5
850	47.8	99.0	239.7	660.7	2000.7
700	3.8	11.6	39.7	151.7	638.2
500	2.5	6.2	16.4	47.0	146.8

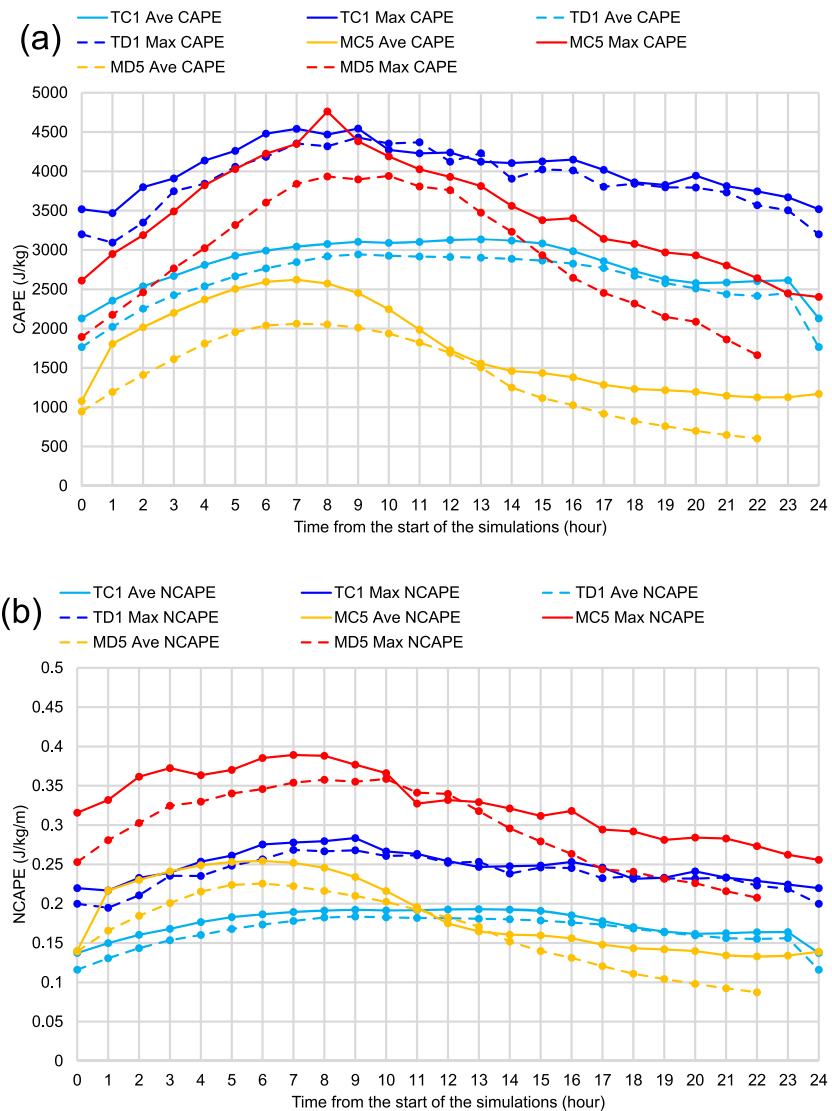


Figure 4. Time series of domain-averaged and maximum values of (a) CAPE and (b) NCAPE calculated in the WRF simulations with the baseline and the reduced vapor (CAPE) configurations for each TWP-ICE and MC3E case. The simulations names in the legends correspond to the abbreviations in Table 1.

domain-averaged and maximum CAPE and normalized CAPE (NCAPE; CAPE divided by the depth from the EL to the LFC) calculated from the baseline and the vapor-reduced (dry) WRF simulations. From the start of the simulations, all CAPE and NCAPE values increase until convection develops. The time variations of CAPE and NCAPE in the MC3E case are larger than those of the TWP-ICE case. The peak values of maximum CAPE of the TWP-ICE and MC3E baseline simulations are similar and $\sim 4,500 \text{ J kg}^{-1}$. However, the peak value of maximum NCAPE in the MC3E case is much larger than that in the TWP-ICE case. This NCAPE difference is attributed to the difference between their atmospheric structure shown in Figure 1, notably a smaller depth between the LFC and EL in MC3E compared to TWP-ICE.

3. Results

3.1. Comparison With MC3E Aerosol Observations

3.1.1. Observed Versus Simulated CCN Concentrations at the ARM SGP Site

The performance of the MERRAero downscaling in calculating CCN concentrations for WRF-SBM is first checked via comparison to CCN measurements at the ARM SGP central facility. Unfortunately, no

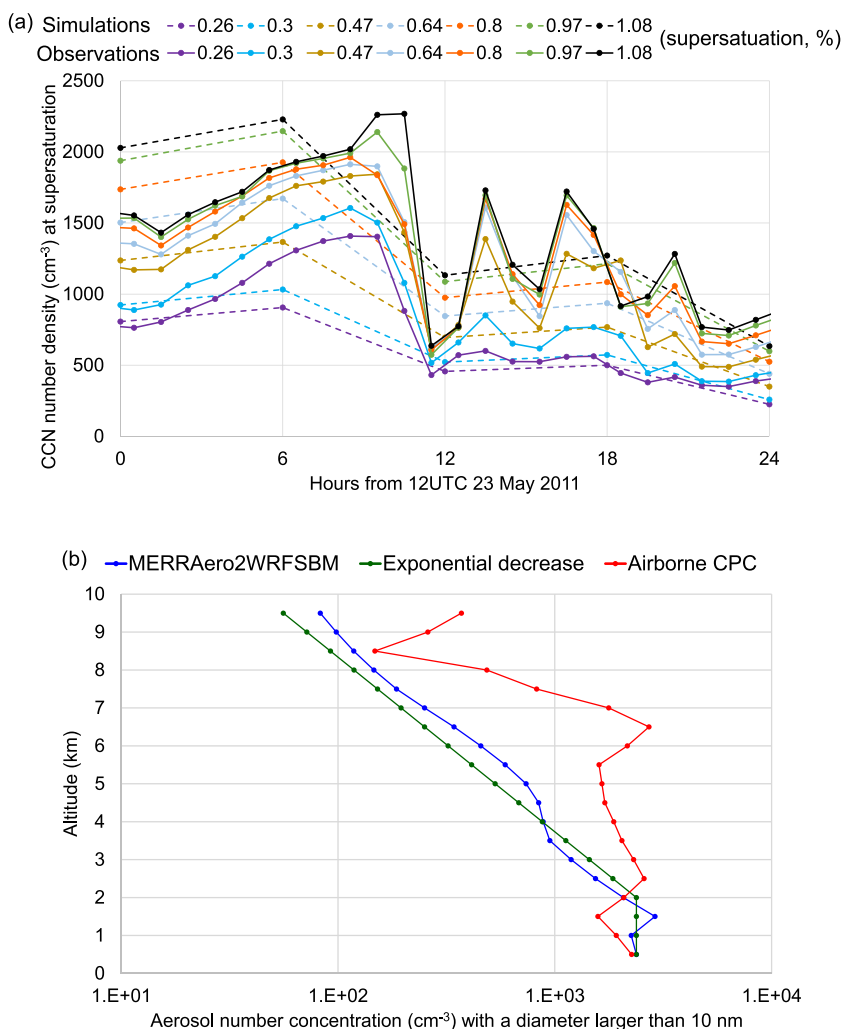


Figure 5. (a) Time series of CCN number concentrations (cm^{-3}) active at the approximate supersaturation values (0.26, 0.3, 0.47, 0.64, 0.8, 0.97, and 1.08%) at the ARM SGP central facility from 12 UTC 23 May 2011 through 12 UTC 24 May 2011, derived from measurements of aerosol observation system (AOS) CCN particle counter (solid lines; 1-hr intervals) and from series of initial conditions for WRF-SBM models downscaled from MERRAero (dotted lines; 6-hr intervals). (b) Vertical profiles of aerosol number concentration (cm^{-3}) with a diameter larger than 10 nm on 23 May 2011. The red, blue, and green lines denote values derived from airborne CPC out-of-cloud measurements (Fridlind et al., 2012, Figure 4), calculated from modeled aerosol fields downscaled from MERRAero through Aero2SBM, and a referential profile with an exponential decrease with increasing altitude (details can be found in text), respectively.

observed CCN data were available from the TWP-ICE field campaign. A time series of CCN number concentrations active at several supersaturations at the ARM SGP central facility is shown in Figure 5a from 12 UTC 23 May through 12 UTC 24 May 2011. The observed values (solid lines in Figure 5a) were derived from ARM aerosol observation system (AOS) CCN particle counter data collected at the SGP central facility site. The modeled CCN number concentrations (dotted lines) were calculated from concentrations of the 65 aerosol variables downscaled from MERRAero to the WRF-SBM simulation and sampled at the lowest vertical level in the atmospheric column, geographically centered in the SGP site.

Figure 5a shows that the modeled CCN number concentrations roughly align with the observed values. Overall, the observed values exhibit high variability between concentrations at lower and higher supersaturations in the time series, while the model values have an almost constant ratio between concentrations at different supersaturations. This discrepancy comes from limitations in the present application of Aero2SBM as well as in GEOS-5 and GOCART used for MERRAero. Changes in PSD of organic

carbonaceous and sulfate aerosols, which are main contributors to continental CCN, are not predicted in GOCART, so those PSDs are totally prescribed in Aero2SBM.

Within the period shown in Figure 5a, the maximum difference between the observed and modeled CCN concentrations is $\sim 1,000 \text{ cm}^{-3}$; at 12 UTC 23 May (the initial time for the WRF MC3E simulations) the difference is $\sim 500 \text{ cm}^{-3}$. Averaging the concentrations every 6 hr (not shown) made the differences between the observed and modeled concentrations smaller compared to Figure 5a, and the maximum difference between the observed and modeled CCN concentrations is $\sim 500 \text{ cm}^{-3}$. These results suggest that a fraction of the differences in Figure 5a may originate from the differences in the record intervals between the CCN observations and the MERRAero, although we cannot be sure that the GEOS-5 simulation for MERRAero captured the temporal variation. The 24-hr averages of the CCN concentrations (Table S1) show the modeled concentration at 1.08% supersaturation is in good agreement with the observed one ($\sim 3\%$ difference), although the differences are larger at smaller supersaturation values. These discrepancies from the observed concentrations may be due to limitations in MERRAero itself and assumptions for aerosol PSD prescribed in Aero2SBM. However, this difference is considerably smaller compared to the difference in representative CCN number concentrations at 1% supersaturation between TWP-ICE and MC3E at 925 and 850 hPa (i.e., the lower troposphere) shown in Tables 2 and 3. Therefore, the downscaled model aerosol fields are sufficiently representative of the continental conditions, and the sensitivity simulations for the maritime and continental CCN loadings are perturbed beyond the peak magnitude of the CCN number concentration error inherited from the aerosol downscaling.

3.1.2. Observed Versus Modeled Aerosol Vertical Profiles

Profiles of aerosol number concentration were observed by the University of North Dakota (UND) *Citation II* using a TSI model 3,010 condensation particle counter (CPC) on 23 May (Fridlind et al., 2012, as a part of the MC3E field campaign). An observed vertical profile of aerosol number concentrations is compared with a profile derived from the downscaled MERRAero aerosol fields for the MC3E 23 May WRF simulations (Figure 5b). The observed values (red line) represent median values over each 1-km layer calculated for out-of-cloud measurements of aerosol number concentration from the CPC (Figure 4 of Fridlind et al. 2017), which counts aerosol particles with diameters exceeding 10 nm. This profile was collected at ~ 21 UTC, over the MC3E domain. The model profile (blue line) represents the vertical distribution of particles with diameters over 10 nm. For reference, Figure 5b includes a vertical profile (green line) starting with the same concentration at 0.5 km of the blue line but exponentially decreasing with increasing altitude above 2 km, which is consistent with a profile conventionally assumed in HUCM SBM (e.g., Khain et al., 1999).

In Figure 5b, the observed aerosol concentrations (red line) are nearly constant from the lowest levels through an altitude of 7 km. Above this level, concentrations are reduced significantly. The modeled values obtained from the MERRAero downscaling (blue line) are close to the observed ones from 0.5 to 2 km, but are significantly less above 2 km. The values of the blue and green lines are similar at all vertical levels and indicate that the model aerosol concentration approximately decreases exponentially with altitude above 2 km. Vertical profiles of aerosol number concentration with an exponential decrease have been similarly adopted in many model aerosol-cloud interaction studies (e.g., Saleeby et al., 2016). However, Figure 5b shows such profiles may not always be representative. A profile obtained from MERRAero dynamic downscaling may not necessarily provide a proper representation either. One possible reason for the MERRAero underprediction in this case is that it may miss enriched Aitken-mode particles transported into or produced in the middle troposphere via gas-to-particle conversion. The assimilation of MODIS-derived reflectances into MERRAero may not be sufficient for correcting vertical profiles of aerosol concentrations. This underprediction of aerosol concentration in the middle troposphere may result in underprediction of CCN concentration at these high levels, although CCN concentrations at these levels are likely less important than those below the cloud base level in the case of deep convection. Nevertheless, it is also possible that the difference between the observations and the model is due to a high variability in the aircraft measurement data. A median vertical profile obtained from multiple MC3E flights does show a linear decrease on a log-scale with increasing altitude (Figure 5 of Fridlind et al., 2012).

3.2. Overviews of the Baseline Simulations and Comparison With Radar Observations

Results of the baseline WRF simulations (TC1 and MC5 in Table 1) are compared to radar observations to confirm that the baseline simulations capture contrasting characteristics in the maritime and continental

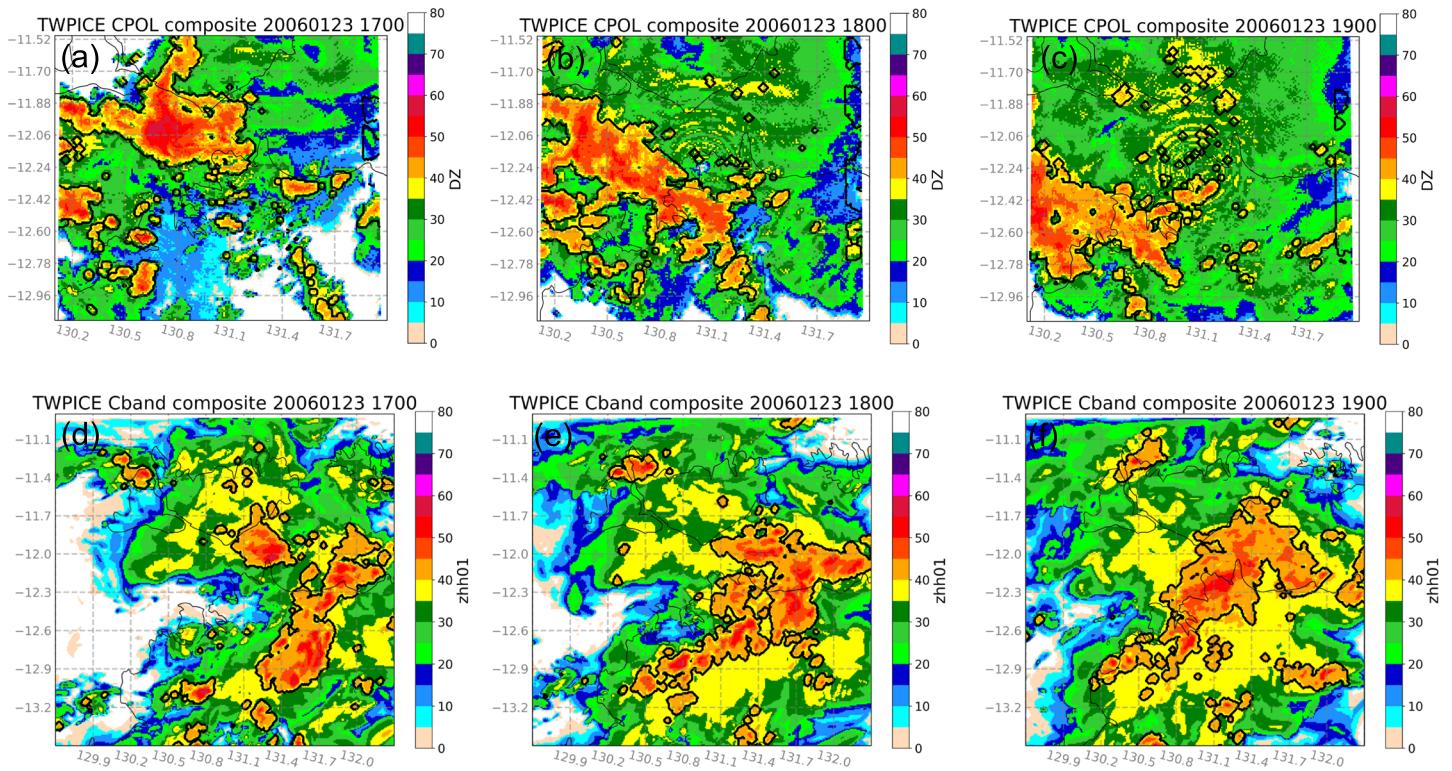


Figure 6. Composite radar reflectivity from the TWP-ICE case, 23 January 2006 at 17, 18, and 19 UTC from (a–c) CPOL observations and (d–f) WRF C-band simulations. Convective area (Steiner et al., 1995) using a convective threshold of 36 dBZ is contoured in black.

deep convective systems in the TWP-ICE and MC3E cases, prior to the sensitivity simulations. Observations from the Bureau of Meteorology (BoM) Darwin C-band polarimetric radar (CPOL) and the DOE polarimetric C-band scanning ARM precipitation radar (CSAPR) are used. Radar variables are compared to corresponding fields computed from the WRF simulations using an offline radar simulator module in the Goddard Satellite Data Simulator Unit (G-SDSU; Matsui et al., 2013, 2019). The method to calculate radar reflectivity follows Masunaga and Kummerow (2005). The particle backscattering cross sections are calculated on the basis of the full solution of Mie-based routine with dielectric constant determined via the Maxwell-Garnet assumption and assuming the particles to be spherical with particle density and size assumed in the SBM for each mass bin. The PSD of hydrometeors as well as rimed mass fractions simulated in the WRF-SBM are input directly into the radar simulator module.

Composite reflectivity (the largest reflectivity in the column at each grid point) at 3 times shows the storm structure and evolution (Figures 6 and 7). The Steiner et al. (1995) radar-reflectivity-based classification algorithm was applied in the same manner to both observations and simulations, using 36 dBZ (40 dBZ) as the convective threshold in TWP-ICE (MC3E). During the time period from 17–19 UTC 23 January 2006, a convective complex was present in the radar domain in both observations (Figures 6a–6c) and simulations (Figures 6d–6f). Both show similar characteristics of convective system that convective areas of irregular shapes and various sizes are surrounded wide stratiform areas. The convective complex evolved into a more linear system that moved west later in the time period, although the orientation of convective complex in the simulations is rotated compared to the observations. The maximum convective reflectivities were larger in the observations (>55 dBZ) compared to simulations (>50 dBZ). Widespread stratiform precipitation encompassed nearly the entire domain in both observations and simulations, although the simulated reflectivities had a larger area >35 dBZ compared to the observations.

As shown in section 2.4.1 (and associated rainfall animations in the supporting information), convective cores over the domain of Figure 6 are elements of a large-scale maritime storm system ~1,000 km in diameter. Thus, it is very difficult to accurately reproduce the position of each convective core within this

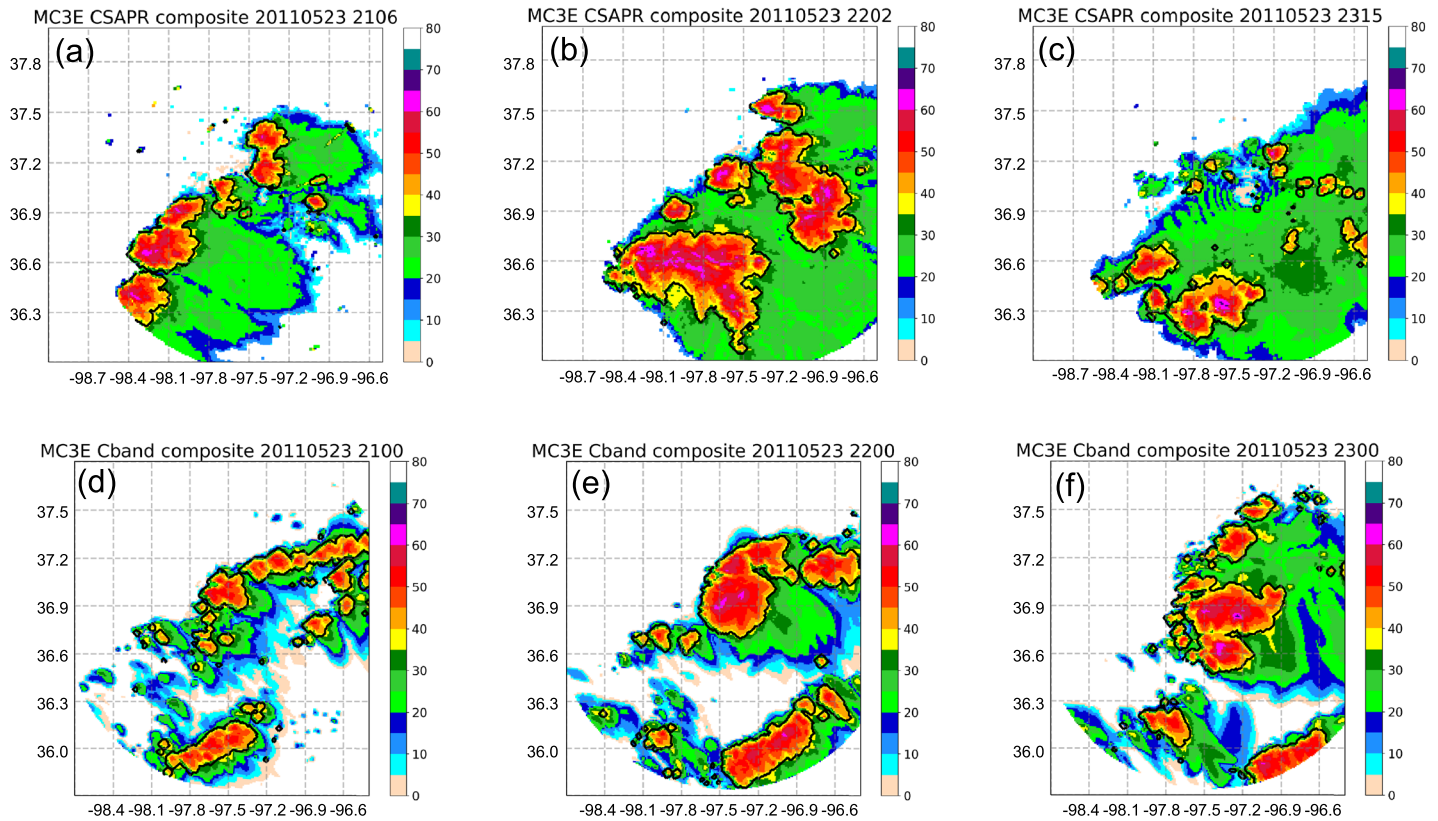


Figure 7. Composite radar reflectivity from MC3E case on 23 May 2011 at ~21, 22, and 23 UTC from (a–c) CSAPR observations and (d–f) WRF C-band simulations. Convective area (Steiner et al., 1995) using a convective threshold of 40 dBZ is contoured in black.

small domain and the current result represents our best effort to reproduce the convective complex as a result of testing the three global reanalysis data sets to drive the simulation. Varble et al. (2014a, 2014b) showed errors in spatial patterns of radar reflectivity in LAM model simulations for the same domain and day, and they suggested that the errors in location and timing of the convective system event might be linked to large-scale forcing biases.

In the MC3E 23 May 2011 case, convective cells with leading stratiform regions organized into MCS features by 2200 UTC, followed by easterly propagation (Figure 7). Maximum observed reflectivities were in excess of 60 dBZ. Large areas of stratiform precipitation (<20 dBZ) were present in the observations (Figures 7a–7c), while stratiform areas were smaller and weaker in the simulation (Figures 7d–7f). This narrower stratiform coverage in model simulation has also been noted in simulations with different cloud microphysics schemes in the same MC3E case (Pu & Lin, 2015). Even though the simulated stratiform areas are smaller in areal coverage, the simulation shows basic characteristics of the observed continental system with clustered convective areas accompanied by stratiform areas, which is distinct from the maritime system.

Figure 8 shows hourly time series of area fractions of radar reflectivity coverage and domain averaged precipitation rates to demonstrate consistency in temporal evolution between the observed and simulated convective systems. Observed precipitation rates were calculated using the polarimetric blended algorithm outlined in Dolan et al. (2013). During TWP-ICE (Figures 8a and 8c), a large fraction of the radar domain was covered by echo, predominantly stratiform, especially after 12 UTC. By 19 UTC, nearly the entire radar domain in both the observations and simulation was covered with echo. In both observations and simulations, the convective area reaches 20% of the domain around 18 UTC, after which the observed convective area decreases while the overall simulated area continues to increase and peaks at 20 UTC before

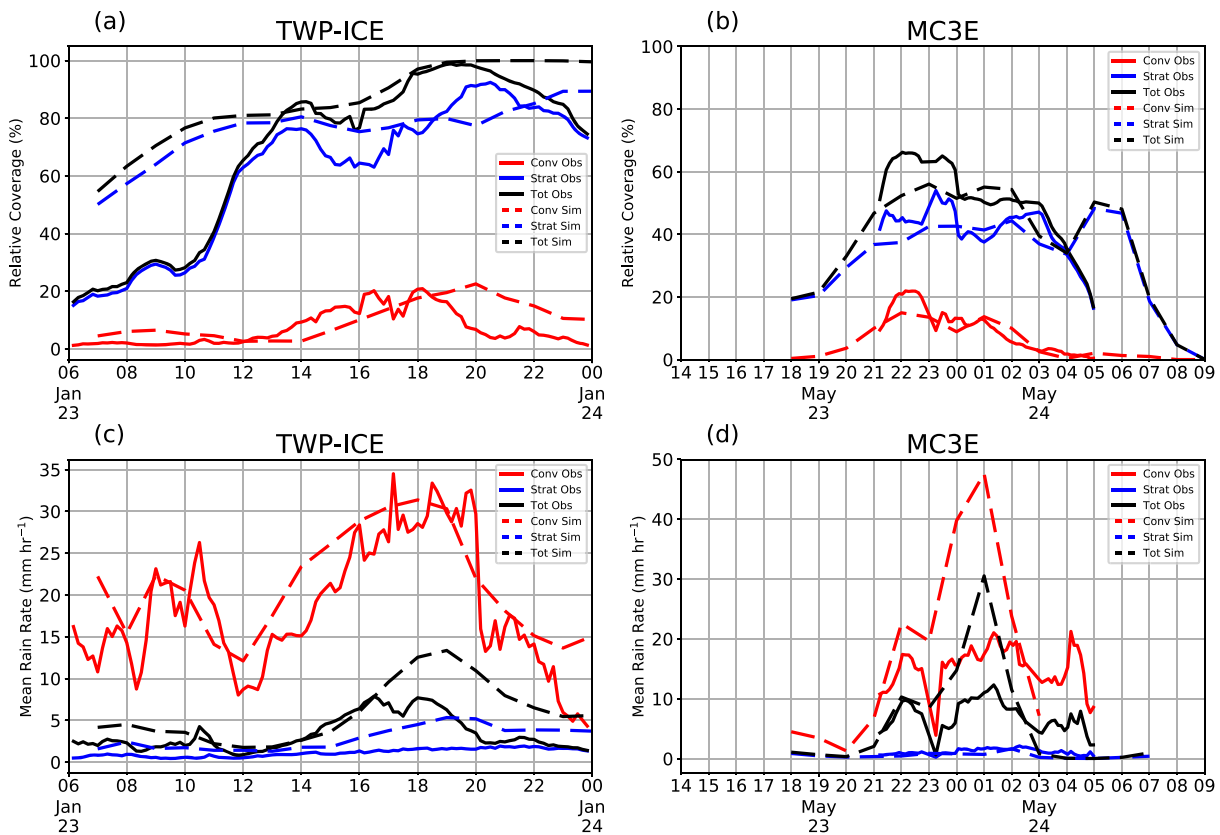


Figure 8. (a) Time series of radar reflectivity coverage ($\text{dBZ} > 0$) and (c) area-averaged mean surface precipitation rate (mm hr^{-1}) for TWP-ICE derived from C-pol radar observations and the WRF baseline simulation; the convective/stratiform types are classified using Steiner reflectivity-based algorithm. (b and d) As in (a) and (c) but derived from SGP CSAPR radar and the WRF baseline simulation for the MC3E case.

decreasing. Average convective rain rates are similar between observations and the simulations, peaking over 30 mm hr^{-1} around 18 UTC before falling off by 20 UTC. Stratiform rain rates were higher (5 mm hr^{-1}) and peak later (19 UTC) in the simulation. Both MC3E time series (Figures 8b and 8d) show that convection entered the radar domain around 21 UTC 23 May 2011 and moved out of the domain by 4 UTC 24 May 2011. The relative echo coverage area is similar between the simulation and observation. However, mean convective precipitation rates were over two times larger in the simulation compared to observations, reaching nearly 50 mm hr^{-1} .

Figure 9 shows observed vertical velocities derived from dual- (TWP-ICE) and multiple-Doppler (MC3E) techniques using the CEDRIC package (Mohr & Miller, 1983) compared to simulated wind fields. The updraft and downdraft percentiles between the observations and simulations were calculated in the same manner employing the same bin spacings and percentiles. Although the grid spacings were similar between them ($\sim 1 \text{ km}$), there are some differences in coverage area that could lead to sampling differences. The observations were constrained to be within the dual-Doppler area, which might not capture all, or even the most intense cores in the domain. The simulations were constrained to the overall radar coverage area, which is larger than the dual-Doppler area. The storm orientation and location may not be exactly as observed during the simulation. The point of these vertical draft profiles is to illustrate in a statistical sense how well represented the convection was by the simulations in comparison to the observations.

During TWP-ICE (Figure 9a), the simulated 99th percentiles were underpredicted in the middle- and low-levels, while 50th percentiles of both observations and simulations were below 1 m s^{-1} . The observations show peak magnitudes around 10-km height above mean sea level (MSL). However, the peaks of the simulated velocities were higher, around 14 km MSL. This discrepancy suggests that the simulated convective system may be more intense locally at upper levels compared to observations.

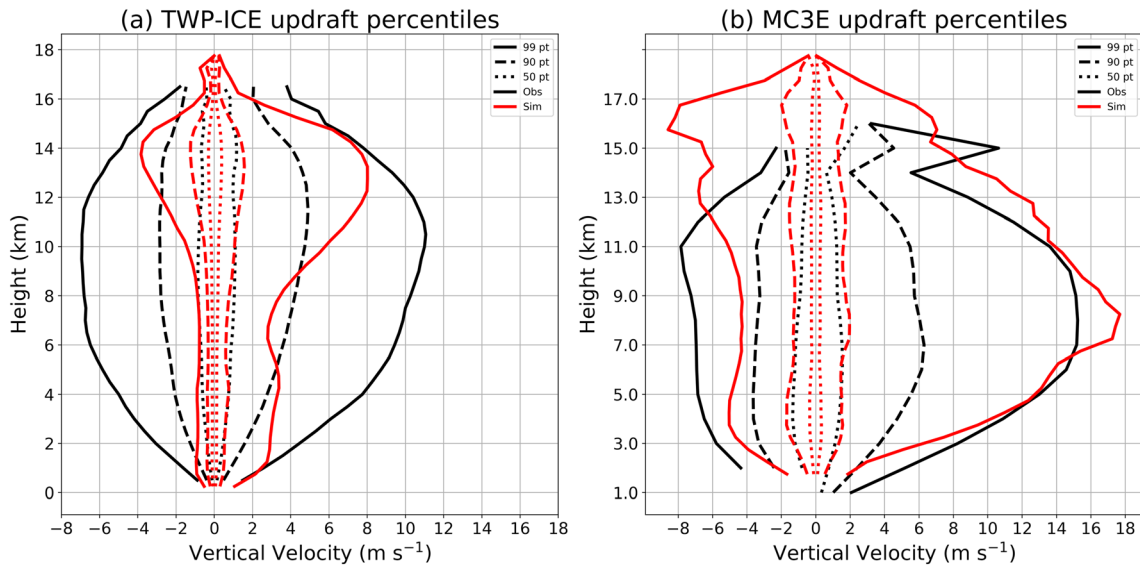


Figure 9. Vertical profiles of the 50th, 90th, and 99th updraft and downdraft percentiles over the radar coverages derived from the radar observations and the model simulations for the (a) TWP-ICE and (b) MC3E cases. The sampling periods are 6–24 UTC 23 January 2006 and 20 UTC 23 May to 06 UTC 24 May 2011.

The vertical profiles of updraft and downdraft percentiles (Figure 9a) are quite different from those shown in Varble et al. (2014a); their Figures 9 and 10). The difference is due to the different sampling criteria. In Varble et al. (2014a), percentile profiles were calculated only for columns with vertical velocities exceeding 1 m s^{-1} from 1 to 15 km in altitude. This biased the sampling to deep convective cores, whereas our percentile profiles are calculated for all positive or negative points without restrictions. The sampling periods are different also, 1310Z–1750Z (around the peak time of strong convection) in Varble et al. (2014a) and 06–24 UTC in ours.

In the MC3E case (Figure 9b), observed and simulated 99th percentile updraft speeds were similar, reaching $14\text{--}16 \text{ m s}^{-1}$ and peaking around 8 km MSL, while downdrafts were smaller in the simulations, except in the upper levels ($> 13 \text{ km}$). Differences above 15 km could be related to relatively few observations at such altitudes. However, 90th and 50th percentiles were smaller in magnitude in simulations compared with observations. Again, the vertical profiles of updraft and downdraft percentiles in this study are different from those shown in Fan et al. (2015); their Figure 7a) for the same MC3E case, because their study sampled only convective cores that were defined by continuous updrafts and reflectivity over certain threshold in columns.

Overall, the model simulations underpredicted the magnitudes of the updraft and downdraft speeds at the 90th and 50th percentiles. Although the grid spacing is similar between the radar measurements and the model simulations ($\sim 1 \text{ km}$), these results suggest that the simulations do not have a fine enough grid spacing to resolve the variability in the observed vertical velocity. Skamarock (2004) showed that the effective resolution of the WRF model was generally 7 times the grid spacing based on the analysis of the kinetic energy spectra. Thus, a finer grid spacing such as several hundred meters is probably required to solve this underprediction.

3.3. Intercomparison of Sensitivity Experiments to the Aerosol and Thermodynamics Perturbations

3.3.1. Surface Precipitation

Here we address initially the response in surface precipitation to both aerosol and thermodynamic perturbations in a series of sensitivity experiments. Table 4 shows the accumulated precipitation amounts averaged over the entire model domains for 24 hr (the entire simulation periods) and the last 18 hr (excluding the 6 hour model spin-up period). The table also includes normalized differences (relative changes) of the accumulated precipitation for both regimes, from that in the lowest CCN loading run in each subset, defined following Equation 7 in SB06:

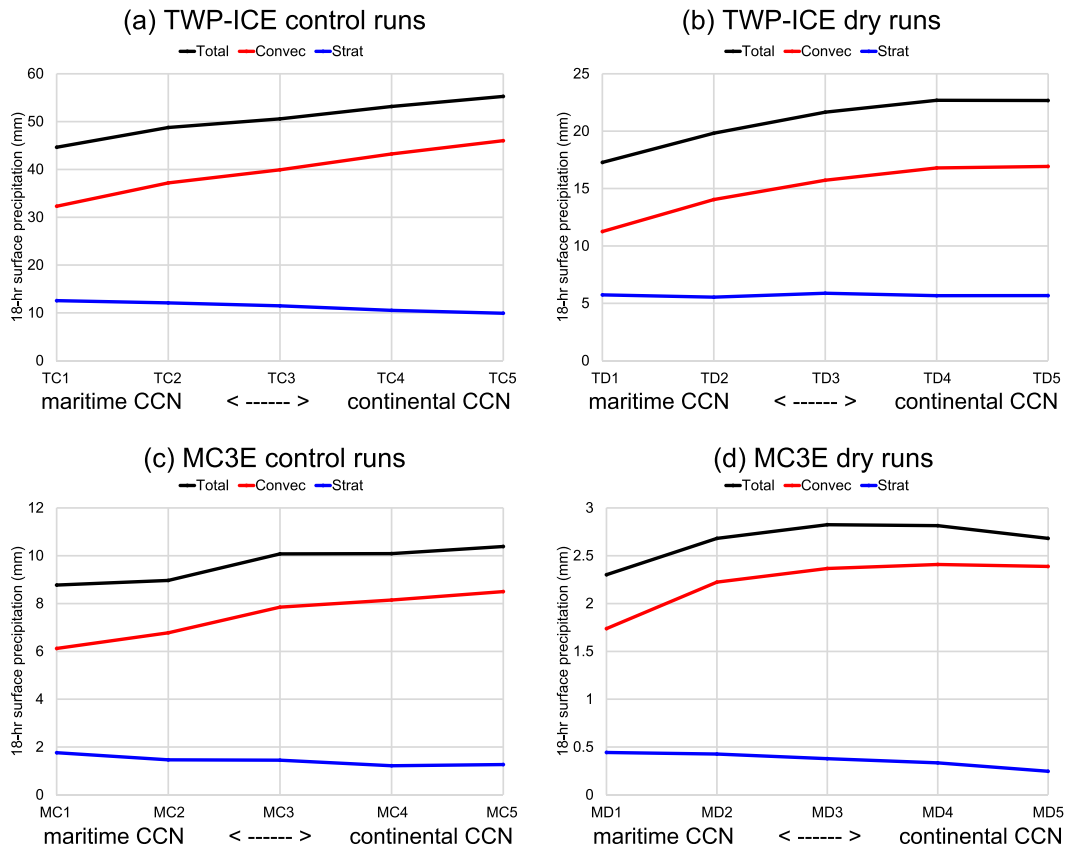


Figure 10. Surface precipitation amounts averaged over the entire model domains for the last 18 hr of the simulation periods in the series of sensitivity experiments. Red and blue lines denote precipitation from convective and stratiform areas (Steiner et al., 1995) to the total (black line), respectively. Note that the y axis scales are different in the plot panels. The x axis labels correspond to experiment abbreviations listed in Table 1 with aerosol concentration perturbing between maritime and continental environments.

$$\Delta P = (P - P_{\text{Lowest}}) / P_{\text{Lowest}}, \quad (1)$$

where P is the precipitation as a function of CCN loading; the subscript, “Lowest,” indicates the value of the lowest CCN loading run, that is, TC1, TD1, MC1, or MD1 in Table 1.

Table 4 shows that the accumulated precipitation in the lowest CCN concentration is the smallest in the five simulations in all four subsets. The change of the CCN loading from the lowest to the highest concentrations causes increases in precipitation amounts by ~15–30%. These increases are similar across the 18–24 hr simulation period. In each subset of the two control-run sets for the TWP-ICE (TC1–5) and MC3E (MC1–5) cases, the precipitation amount is the highest in the highest CCN loading run (TC5 and MC5), and the values increase monotonically in response to CCN increases through the intermediate runs. In each subset of the dry-run (reduced CAPE) simulations, interestingly, an intermediate run (TD4 and MD3) yields the largest surface precipitation. Evidently, with reduced CAPE, the impact of increasing CCN differs as the monotonic increase is disrupted. The highest CCN loading run in TWP-ICE dry (TD5) produces a precipitation amount similar to that of TD4, while MD5 has considerably less surface precipitation compared to MD3 and MD4. The reduction rates of the precipitation due to the CAPE change are ~60% in the TWP-ICE runs and 70% in the MC3E runs. These rates tend to be larger in the lowest and highest CCN loadings and smallest in an intermediate in both the TWP-ICE and MC3E cases.

The normalized differences (relative changes) of accumulated precipitation in Table 4 are compared to those derived from many previous modeling studies listed in Table 1 of Tao and Li (2016). A few studies show positive values of the order of 10% that are similar to those obtained in this study. Tao et al. (2007) and Lee et al. (2008a, 2008b, 2009) simulated tropical maritime (The Tropical Ocean-Global Atmosphere Coupled

Table 4

Accumulated Precipitation of Sensitivity Simulations for the TWP-ICE and MC3E Cases (Table 1) Averaged Over the Simulation Domains for the 24 hr and the Last 18 hr and Their Relative Change in % From Those in Simulations With the Lowest CCN Loading Condition (TC1, TD1, MC1, and MD1) (Equation 1)

Simulations	24-hr precip. (mm)	24-hr relative change (%)	18-hr precip. (mm)	18-hr relative change (%)
TC1	48.860	0.0	44.637	0.0
TC2	53.604	9.7	48.770	9.3
TC3	55.770	14.1	50.575	13.3
TC4	58.764	20.3	53.162	19.1
TC5	60.958	24.8	55.273	23.8
TD1	18.623	0.0	17.278	0.0
TD2	21.258	14.1	19.821	14.7
TD3	23.220	24.7	21.654	25.3
TD4	24.318	30.6	22.691	31.3
TD5	24.251	30.2	22.671	31.2
MC1	8.904	0.0	8.774	0.0
MC2	9.104	2.3	8.966	2.2
MC3	10.225	14.8	10.079	14.9
MC4	10.236	15.0	10.089	15.0
MC5	10.531	18.3	10.387	18.4
MD1	2.302	0.0	2.302	0.0
MD2	2.682	16.5	2.682	16.5
MD3	2.825	22.7	2.825	22.7
MD4	2.815	22.3	2.815	22.3
MD5	2.682	16.5	2.682	16.5

Note. Values exhibiting monotonic increase or decrease in series of runs in each subset are represented by bold fonts.

Ocean Atmosphere Response Experiment; TOGA COARE) and mid-latitude continental (ARM SGP) cases, respectively. Although these two studies are based on two-dimensional model simulations, the precipitation sensitivities we find are in agreement with these studies, lending confidence to our results.

The normalized differences of the accumulated precipitation (Table 4) are also compared with those obtained in SB06, Storer et al. (2010), and Grant and van den Heever (2015), in which aerosols and vapor (consequently CAPE) were perturbed simultaneously. These three modeling studies basically follow the simulation design in Weisman and Klemp (1982, 1984); the forms of the simulated convective systems vary according to vapor content and wind shear. In SB06, the normalized precipitation difference for increasing CCN is positive for multicell systems (higher CAPE and weaker wind shear) and negative for both single, ordinary cells (lower CAPE and weaker wind shear), and supercells (stronger wind shear); the results in the other two studies roughly follow these findings. Our simulated systems are multicellular convection (Figures 6 and 7), and the positive values of the normalized difference (Table 4) are consistent with those in SB06. However, the decreases in vapor (consequently CAPE) in our study do not lead to a change from positive to negative normalized differences as shown in Figure 12a of SB06. Perhaps the vapor perturbation in our study is sufficiently small that the system stays in a range of positive normalized differences (upper left part of Figure 12a of SB06).

The changes in surface precipitation are further investigated using convective and stratiform precipitation separation based on Steiner et al. (1995). This investigation is motivated by analysis of surface rain rate PDFs (not shown), in which the probability of weak (strong) surface rainfall rates decreases (increases) with increasing CCN concentration. The domain-averaged surface precipitation amounts from convective and stratiform areas averaged for the last 18 hr of the simulation are shown in Figure 10; the amounts and their relative changes (Equation 1) are also listed in Table S2 in the supporting information. The precipitation amounts in convective areas generally increases with increasing CCN. The change in the CCN loading from the lowest to the highest concentrations yields an increase of the precipitation within convective areas by ~40–50% (Figure 10 and Table S2). However, precipitation within stratiform areas stays approximately constant or substantially decreases. The reduction rates are ~0–40%, and the changes largely differ according to the selection of the TWP-ICE or MC3E case and the control or dry (reduced CAPE) simulations. The changes in the total precipitation (black lines in Figure 10) generally follow those in the convective precipitation (red lines), because the precipitation amounts in convective areas are considerably larger than those from stratiform areas (blue lines).

The changes in convective and stratiform precipitation areal coverages are shown in Figure 11 in the form of the percentages to the TWP-ICE or MC3E model domain averaged for the 18 hr. Unlike the changes in the surface precipitation amount or rate (Figure 10 and Tables 4 and S2), the responses to the CCN loading perturbations differ considerably depending on the cases and the types of simulations. Relative changes (Equation 1) vary within a range of $\pm 20\%$. In the TWP-ICE runs, the reduction in CAPE yields the opposite response of the changes in convective and stratiform precipitation areas to the CCN loading perturbations: both convective and stratiform precipitation areas decrease slightly in the control runs with higher CCN loadings, while those areas tend to increase in the CAPE-reduced runs. However, the MC3E runs show a similar response of the changes in convective and stratiform precipitation areas in the control and CAPE-reduced simulations: the convective area shows non-monotonic changes, while the stratiform area roughly decreases by ~20% in the relative change.

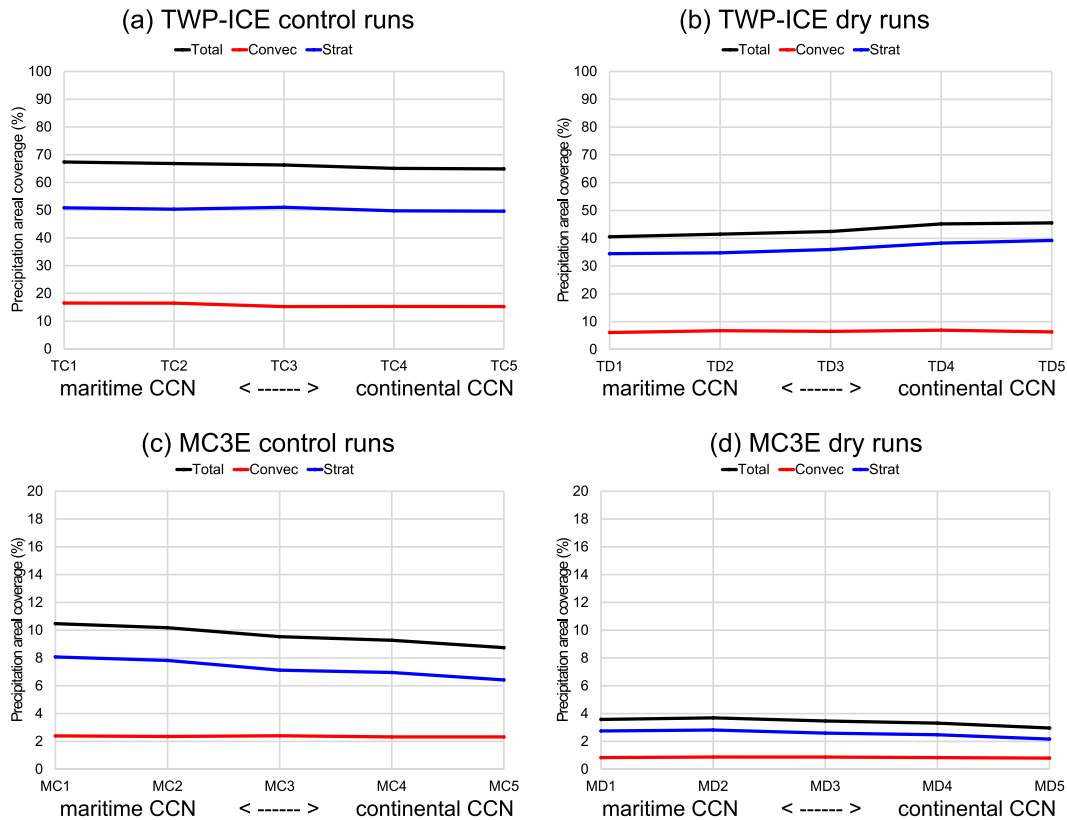


Figure 11. Percentages of precipitation areal coverages in the entire model domains averaged for the last 18 hr of the simulation periods in the series of sensitivity experiments. Red and blue lines denote convective and stratiform precipitation areas (Steiner et al., 1995) to the total (black line), respectively. Note that the y axis scales are different in the plot panels. The x axis labels correspond to simulation name abbreviations listed in Table 1 with aerosol concentration perturbing between maritime and continental environments.

The hourly variations of the convective and stratiform precipitation areal coverages and the surface precipitation rates (Figure S2 in supporting information) indicate that general features of the development of the convective systems are not strongly affected by the variation in the CCN loading, at least over the current short integration periods. This result supports that time- and domain-averaged values shown in Tables 4 and S2 and Figures 10 and 11 work as metrics that are suitable to represent the sensitivity of the convective systems to the CCN and CAPE perturbations.

3.3.2. Cloud Microphysics and Vertical Motions

Discussion on the response to the CCN loading changes is extended to cloud microphysics as well as updraft and downdraft statistics. Hourly variations of domain-averaged vertically integrated mass concentration (i.e. water paths of hydrometeor particles) are similar to each other in each subset of sensitivity experiments (Figures S3 and S4). Therefore, comparing time averages of these water paths is an effective means to evaluate overall changes in the concentration of each hydrometeor type in response to the CCN changes.

Table 5 shows time and domain averages of the water path of each hydrometeor type for the last 18 hr of the simulation periods in the form of their relative changes (Equation 1). The monotonic increase in hail in response to increasing CCN loading is highlighted in all four subsets in the sensitivity simulations, although the amounts of hail are negligible compared to those of other hydrometeor types in the TWP-ICE case (Figure S3). This increase in hail is consistent with the hypothesis suggested by Rosenfeld et al. (2008): Higher CCN loading conditions promote more supercooled water above the freezing level, aiding the development of rimed particles such as hail and graupel.

Overall increase in cloud ice in Table 5 may be related to the freezing of supercooled water, although the MC3E dry runs do not show a monotonic increase. MD3 and MD4 show larger accumulated surface precipitation than MD5 (Table 4). Supercooled water and cloud ice in MD3 and MD4 may be consumed more efficiently for rain production than in MD5.

Table 5
Time- and Domain-Averaged Water Path of Each Hydrometeor Type in the Sensitivity Simulations for the TWP-ICE and MC3E Cases (Table 1) Over the Simulation Domains for the Last 18 hr of the Simulation Periods, Represented in the Form of Their Relative Change in % From Those in Simulations With the Lowest CCN Loading Condition (Equation 1)

Simulations	Liquid	Cloud ice	Snow	Graupel	Hail	Total
TC1	0.0	0.0	0.0	0.0	0.0	0.0
TC2	6.4	7.6	-5.3	24.8	18.6	6.0
TC3	7.8	21.0	-18.7	32.9	94.9	5.7
TC4	7.3	45.9	-17.8	5.0	233.9	4.9
TC5	8.3	49.8	-18.3	4.8	288.1	5.7
TD1	0.0	0.0	0.0	0.0	0.0	0.0
TD2	10.0	17.3	2.9	42.0	44.4	13.2
TD3	14.7	38.8	-4.4	80.1	122.2	21.4
TD4	14.8	70.1	3.2	26.7	294.4	22.7
TD5	13.8	84.1	-4.5	26.8	361.1	22.5
MC1	0.0	0.0	0.0	0.0	0.0	0.0
MC2	0.0	5.5	-4.3	-31.3	44.4	-13.8
MC3	5.7	16.1	0.4	-47.4	130.0	-16.6
MC4	2.0	24.2	-7.8	-55.2	185.5	-19.8
MC5	5.9	50.8	-9.1	-58.2	263.7	-14.3
MD1	0.0	0.0	0.0	0.0	0.0	0.0
MD2	2.8	17.3	12.0	-23.6	84.4	-6.3
MD3	2.4	10.8	9.6	-48.8	193.8	-19.8
MD4	0.8	16.0	6.3	-55.9	262.5	-22.4
MD5	-2.6	18.4	-10.2	-61.2	315.6	-26.6

Note. Values exhibiting monotonic increase or decrease in series of runs in each subset are represented by bold fonts.

The changes in graupel are different between the TWP-ICE and MC3E simulations (Table 5). Graupel monotonically decreases in the two subsets of the MC3E case. In the TWP-ICE case, however, graupel increases from the lowest CCN loading runs (TC1 and TD1) through the other runs, although the increases are not monotonic. Since little hail form in the TWP-ICE case, graupel is the main consumer of supercooled cloud water.

To extend the discussion on the changes reported in Table 5, Figures 12 and 13 show vertical profiles of relative changes (Equation 1) in mixing ratios of the hydrometeor particle types. The mixing ratios are conditional means over the convective (Figure 12) and stratiform precipitation areas (Figure 13) based on the classification of Steiner et al. (1995). The original mixing ratio vertical profiles are shown in Figures S5 and S6 in the supporting information.

Overall, the control and modified-CAPE runs share similar features in both TWP-ICE and MC3E cases (Figures 12 and 13). The profiles of cloud water (q_c) show monotonic increases in response to the increases in CCN loading in all subsets of the simulations for both convective and stratiform precipitation regions, especially at levels close to freezing level heights (~4.5 km in the TWP-ICE case and 4 km in the MC3E case). The changes in rain (q_r) are different in the convective and stratiform precipitation areas; particularly, rain mixing ratios decrease in stratiform areas with increasing CCN. The changes in cloud ice (q_i) are characterized by significant increases at upper levels and slight decreases at middle levels in both convective and stratiform areas. Upper level increases are associated with freezing of increased supercooled water at low temperatures. The profiles in snow (q_s) changes are different in the TWP-ICE and MC3E cases. The

TWP-ICE runs show overall decreases in convective areas and increases in stratiform areas, although these changes are modest at best. The MC3E runs show slight decreases at most levels above the freezing heights, while slight increases occur in the midlevels in both convective and stratiform areas. The changes in graupel (q_g) in the TWP-ICE runs show interesting structures at upper levels in both convective and stratiform precipitation areas: Graupel increases in TC2–3 and TD2–3 and decreases in higher levels in TC4–5 and TD4–5. However, the MC3E runs show a different trend in the changes in graupel, that is, overall decreases at most levels above the freezing level heights.

Vertical profiles of updraft and downdraft statistics in the sensitivity simulations are shown in Figures 14 and 15 separately for convective and stratiform precipitation areas in the form of 50th, 90th, and 99th percentiles. In convective areas in the TWP-ICE control and dry runs, these updraft (downdraft) percentiles increase (decrease) monotonically with increasing CCN. These changes in vertical velocity are due to changes in latent heating through cloud microphysical processes and buoyancy, which are discussed in the next subsection. The positive (negative) responses in the percentiles are disrupted in convective areas in the MC3E control and dry runs as well as stratiform areas in all runs. In particular, MC3E runs show complicated structures wherein relative magnitudes of the percentiles are quite different in most vertical levels.

3.3.3. Latent Heating Budget

Khain et al. (2009) analyzed the mass and heat budgets in sensitivity simulations for various cloud simulations to classify the effects of the change in aerosol loading on the precipitation. Following Khain et al. (2009), Figure 16 shows vertical profiles of domain-averaged temperature change averaged over the whole simulation periods due to latent heating and cooling in our sensitivity experiments; Figures S7 and S8 in the supporting information illustrate profiles of six heating/cooling components (condensation, evaporation, deposition, sublimation, freezing, and melting). Overall, the appearances of the vertical profiles in the control and dry runs in each TWP-ICE and MC3E case are similar. The vertical profiles of the control and dry runs in the TWP-ICE case (Figures 16a and 16c) are generally characterized by monotonic changes for the CCN loading changes. Heating, cooling, and net profiles generally increase with CCN increases, except

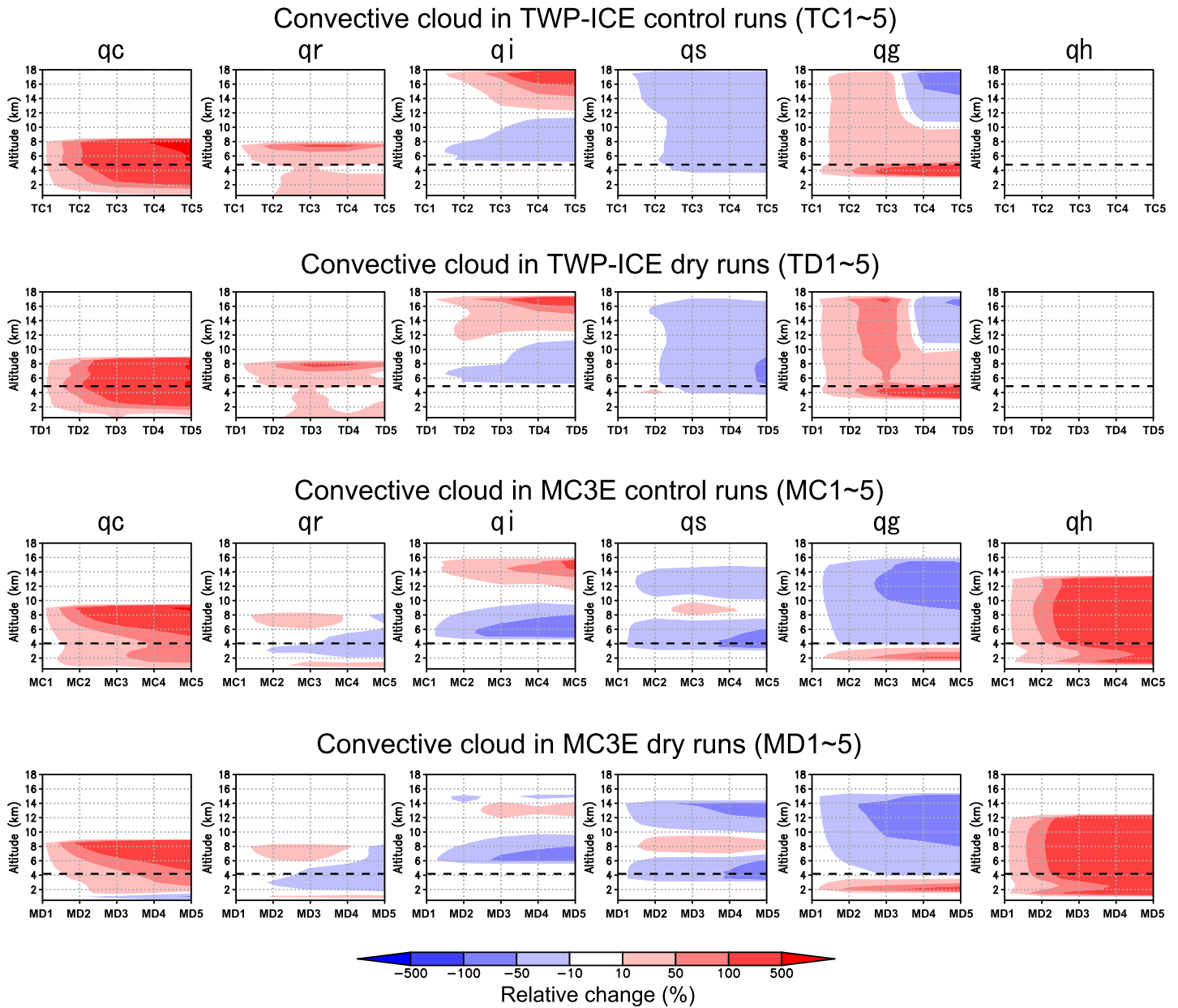


Figure 12. Vertical profiles of relative changes (Equation 1) in mixing ratios of the hydrometeor types (q_c : Cloud water, q_r : Rain, q_i : ICE crystals, q_s : Snow, q_g : Graupel, and q_h : Hail). The mixing ratio is the conditional mean over convective precipitation areas (Steiner et al., 1995). The relative changes are masked-out for mixing ratios less than 10^{-5} (kg kg^{-1}) in the lowest CCN run. The threshold particle radius between the cloud water (q_c) and rain (q_r) is $\sim 90 \mu\text{m}$. The black dashed lines denote approximate altitudes of 0°C isotherm (4.7 km in TWP-ICE and 4 km in MC3E cases).

for a decrease in cooling below ~ 1 km height and slightly larger net budget in TD4 than that in TD5 at several heights. In contrast, the vertical profiles of the MC3E runs (Figures 16b and 16d) are more complicated. The heating and cooling, particularly cooling from 4 km through 8 km heights, change nonmonotonically in response to the CCN changes. Profiles of net heating show overall increases below 5 km and decreases around 8 km when CCN concentrations increase, which are attributed to the changes in condensation and deposition heating at these heights, respectively (Figures S7).

The vertical profiles of latent heat budgets from our TWP-ICE and MC3E simulations in Figure 16 share characteristics with those in Khain et al. (2009) for the GATE-74 deep maritime cloud simulation (Figure 4 in Khain, 2009, and Khain et al., 2004) and for a midlatitude hail storm in southern Germany (Figure 14

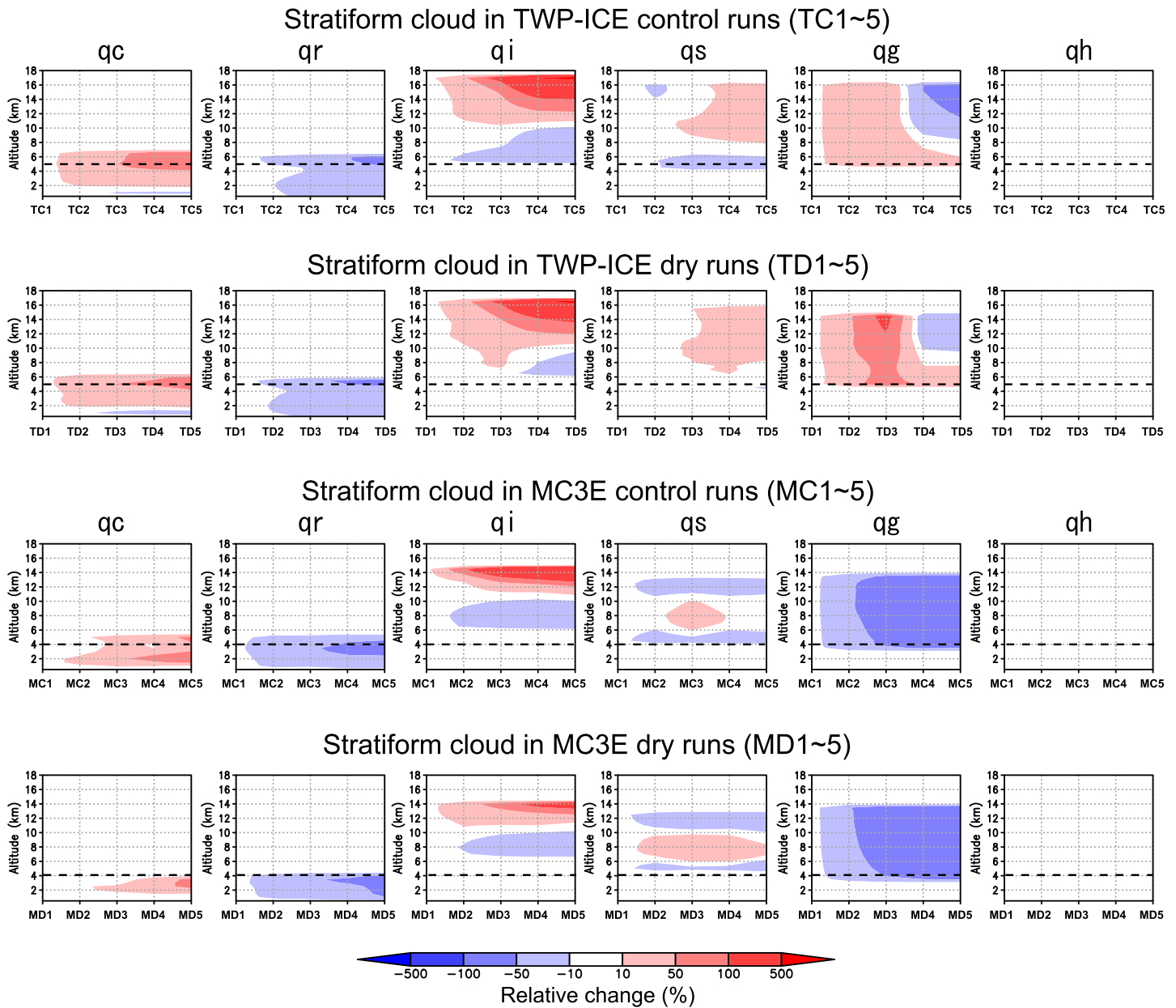


Figure 13. As in Figure 12 but for stratiform precipitation areas.

in Khain, 2009, and Khain et al., 2011), respectively. The former is characterized by increases in heating, cooling and net heating for the change from maritime through continental CCN conditions. In humid conditions like our maritime cases, increases in aerosol concentrations cause increases in the net condensate generation, which could lead to increase in precipitation (Khain, 2009). The latter is characterized by relatively complicated profiles with increase in the net heating budget in most middle vertical levels and decreases in limited upper levels with increasing CCN concentrations.

The changes in updraft and downdraft structures (Figures 14 and 15) are attributable to the changes in the total buoyancy as a result of competition between thermal buoyancy and condensate loading (e.g., Fan et al., 2017); changes in the thermal buoyancy are tied to the changes in the latent heating and cooling budgets (Figure 16). The competition between the thermal buoyancy and condensation loading effects in convective regions are evaluated (plots are not shown) based on Equation 2 of Fan et al. (2017). The thermal

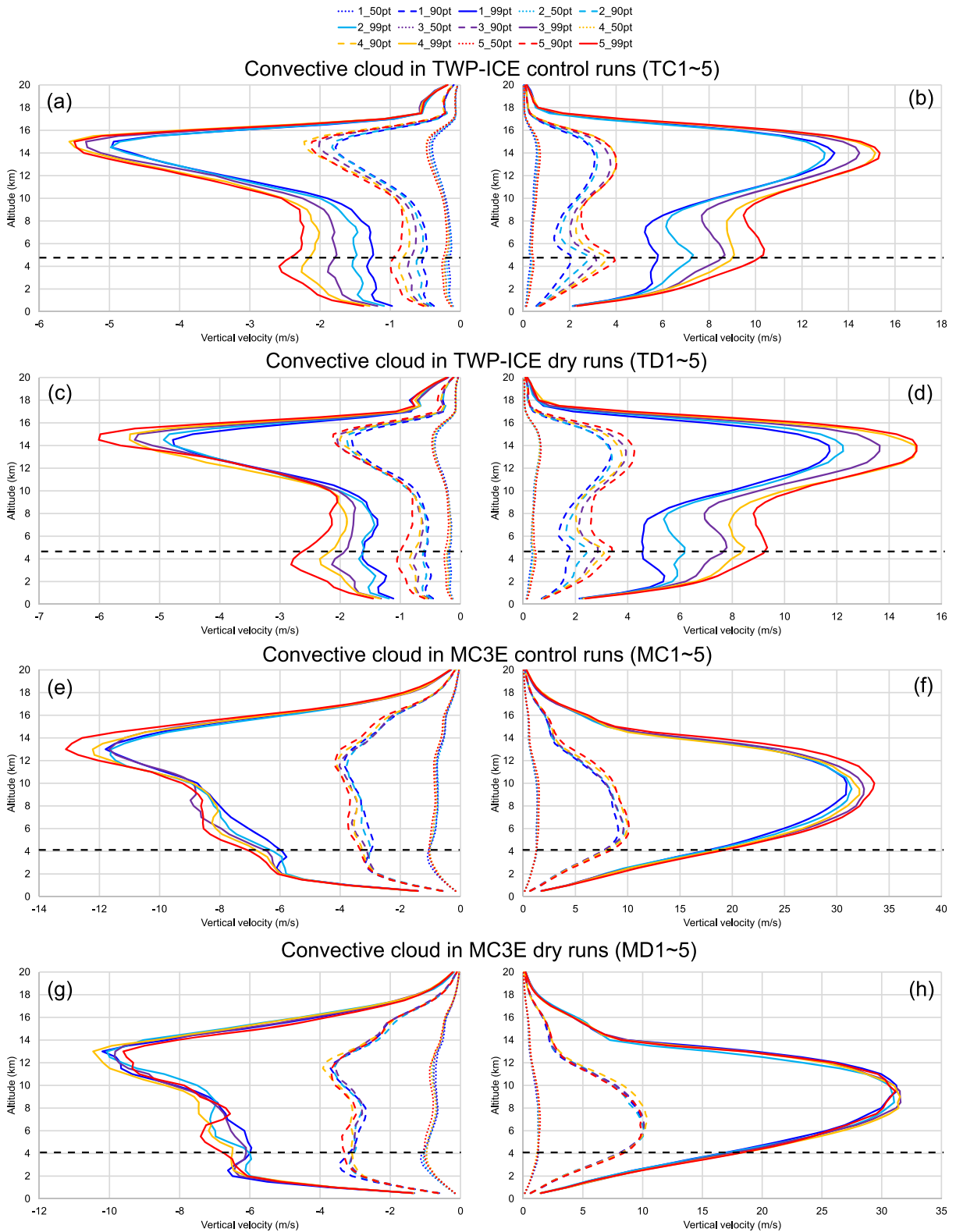


Figure 14. Vertical profiles of the 50th, 90th, and 99th updraft and downdraft percentiles over convective precipitation areas (Steiner et al., 1995) in the sensitivity simulations. The sampling is over the entire simulation domains for the last 18 hr (except for the first 6 hr as a spin-up time). The numbers in the graph legend correspond to the last digits of the sensitivity experiment abbreviations in Table 1, which show relative magnitude in the aerosol concentrations in the experiment configurations, and denote the ordinal numbers of the percentiles. The black dashed lines denote approximate altitudes of 0°C isotherm.

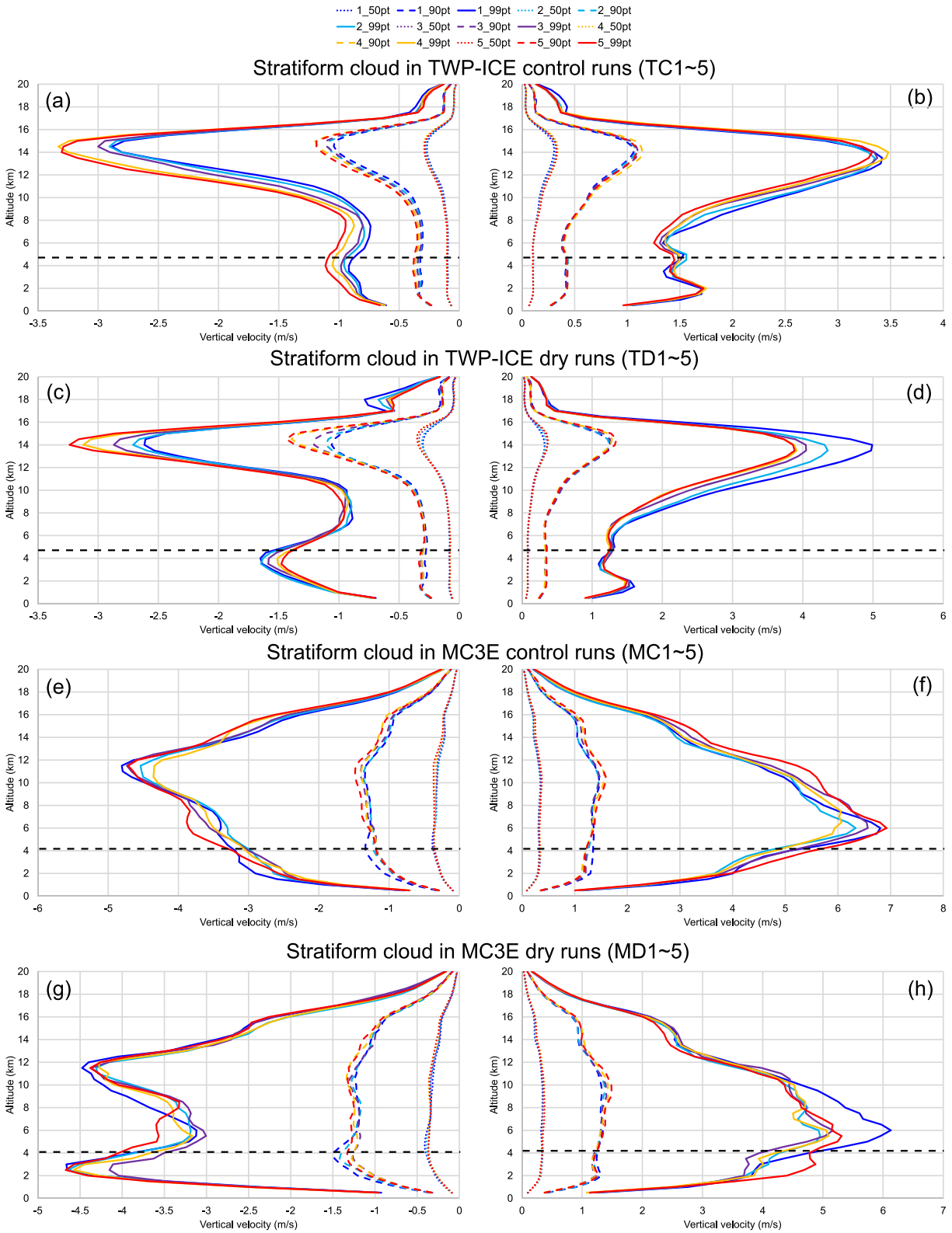


Figure 15. As in Figure 14 but for stratiform precipitation areas.

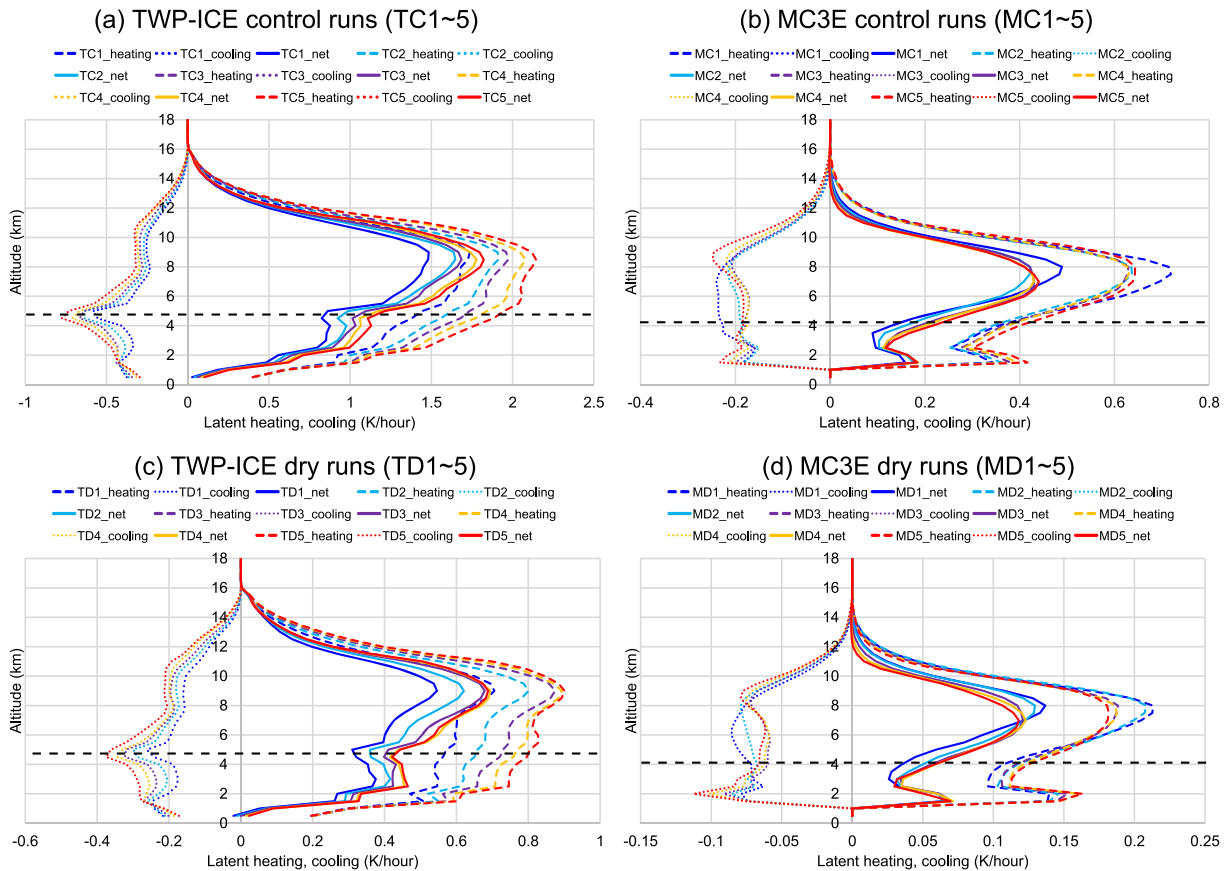


Figure 16. Vertical profiles of horizontally-averaged temperature change (K hr^{-1}) due to latent heating/cooling calculated for the entire simulation periods. The black dashed lines denote approximate altitudes of 0°C isotherm. The altitudes near the surface in the MC3E case are excluded in the calculation (all values are zero) to remove the influence of grid points under the orographic heights. The simulation name abbreviations in the graph legends are listed in Table 1.

buoyancy overall overwhelms the condensation loading effects, and the changes in the total buoyancy follows the changes in the thermal buoyancy. Thus, the changes in latent heating and cooling have large impact on the updraft and downdraft structures. The monotonic increases in heating and cooling in the TWP-ICE runs with increases in CCN concentrations are consistent with monotonic increases in updrafts and downdrafts, especially in convective precipitation areas. This positive correlation is not evident in stratiform areas, particularly in the TWP-ICE dry runs wherein 99th updraft percentiles decrease with increasing CCN concentrations. In contrast, both heating/cooling and up/downdrafts change in complex ways in those MC3E runs, which is caused by consistent with relatively complicated profiles of heating and cooling.

Figure 14 shows that the increase in updrafts in the convective regions with increasing CCN in the TWP-ICE simulations is significant at 2–8 km altitudes across the freezing level. These updraft increases are attributable to the increase in condensation heating at these levels (Figure S7). The increase in condensation heating is simulated even for the first few hours from the start of the simulations (not shown), in which feedback due to evaporative cooling through cool pool formation is not significant. Thus, these results suggest that the increase in the updrafts is due to the warm-phase invigoration process. This is consistent with Fan et al. (2018). In contrast, the same analysis for the first few hours (also not shown) illustrates that the warm-phase invigoration is not effective in the MC3E simulations. The increase in condensation heating near the surface is simultaneous with evaporation cooling at the same levels (Figures S7 and S8). The difference between the TWP-ICE and MC3E simulations is attributable to the difference in humidity below the freezing level (Figure 1). The dry condition below the freezing level in the MC3E case is unsuitable to the warm-phase invigoration process.

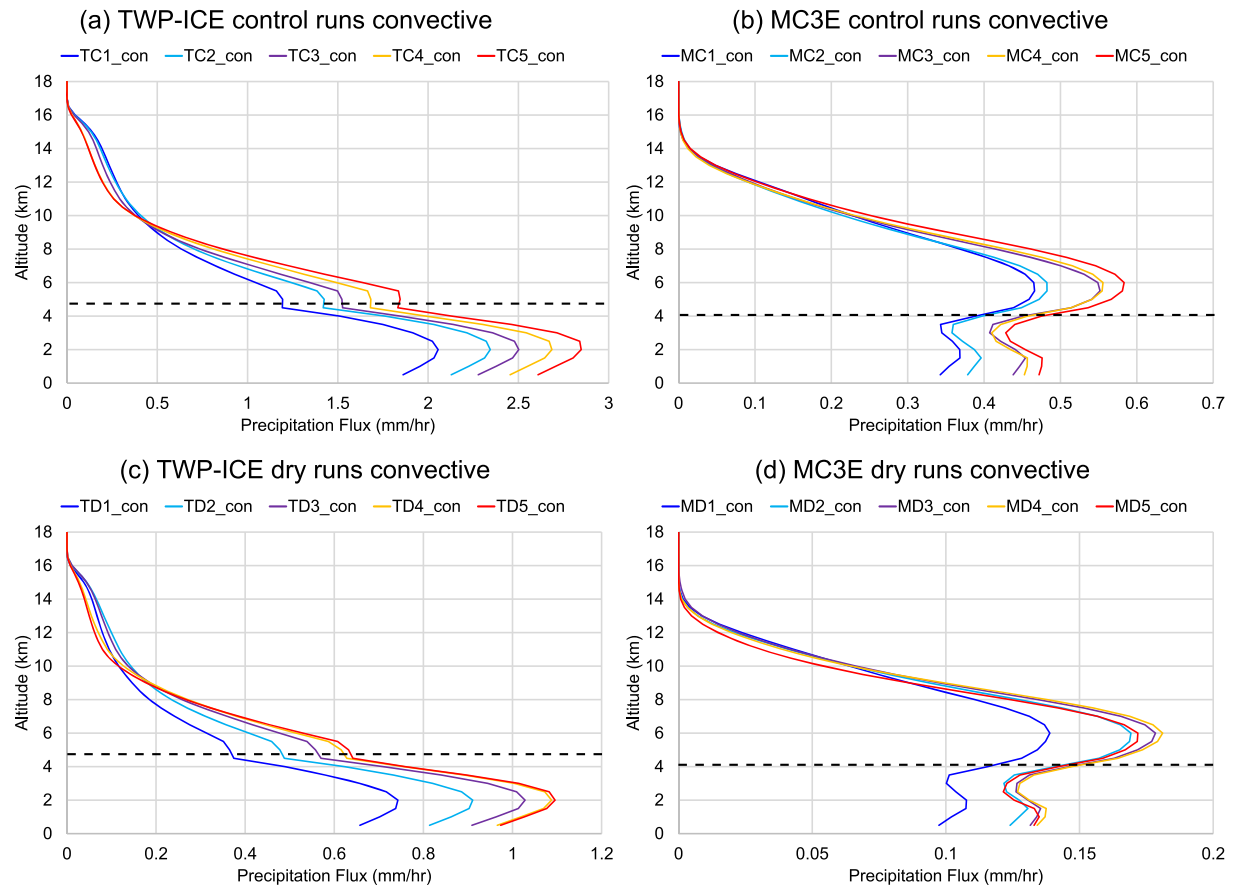


Figure 17. Vertical profiles of precipitation flux (mm hr^{-1}) in convective precipitation areas averaged over the entire model domains for the last 18 hr of the simulation periods. The black dashed lines denote approximate altitudes of 0°C isotherm. The simulation name abbreviations in the graph legends are listed in Table 1.

4. Discussion

4.1. Differing Sensitivity of Convective and Stratiform Precipitation to CCN Changes

In the results shown in section 3.3.1, the surface precipitation rates in convective and stratiform precipitation areas show different sensitivity to the CCN concentration changes in both TWP-ICE and MC3E simulations. This subsection analyzes these changes in more detail. Figures 17 and 18 illustrate vertical profiles of time- and domain-averaged downward precipitation flux calculated from predicted hydrometeor PSD and its terminal fall velocity in convective and stratiform precipitation areas, respectively. They are comparable to surface precipitation rates.

In the convective precipitation areas (Figure 17), the differences in the precipitation fluxes (with CCN changes) above the freezing level are consistent with those below; this characteristic is same across all sets of the TWP-ICE/MC3E and control/dry runs. Thus, processes above the freezing level (mostly mixed-phase processes) control the surface precipitation changes in the convective precipitation areas. Figure 12 shows that these increases in the precipitation fluxes above the freezing level with increasing CCN concentrations are attributable to the increases in graupel in TWP-ICE and to hail in MC3E. An opposite effect was found in stratiform precipitation areas. For the TWP-ICE and MC3E simulations (Figure 18), the precipitation fluxes decrease with increasing CCN concentrations. Evidently, heavier convective rainfall reduces the amount of hydrometeors advected into the stratiform region, leading to lesser amounts of stratiform precipitation with increasing CCN concentrations.

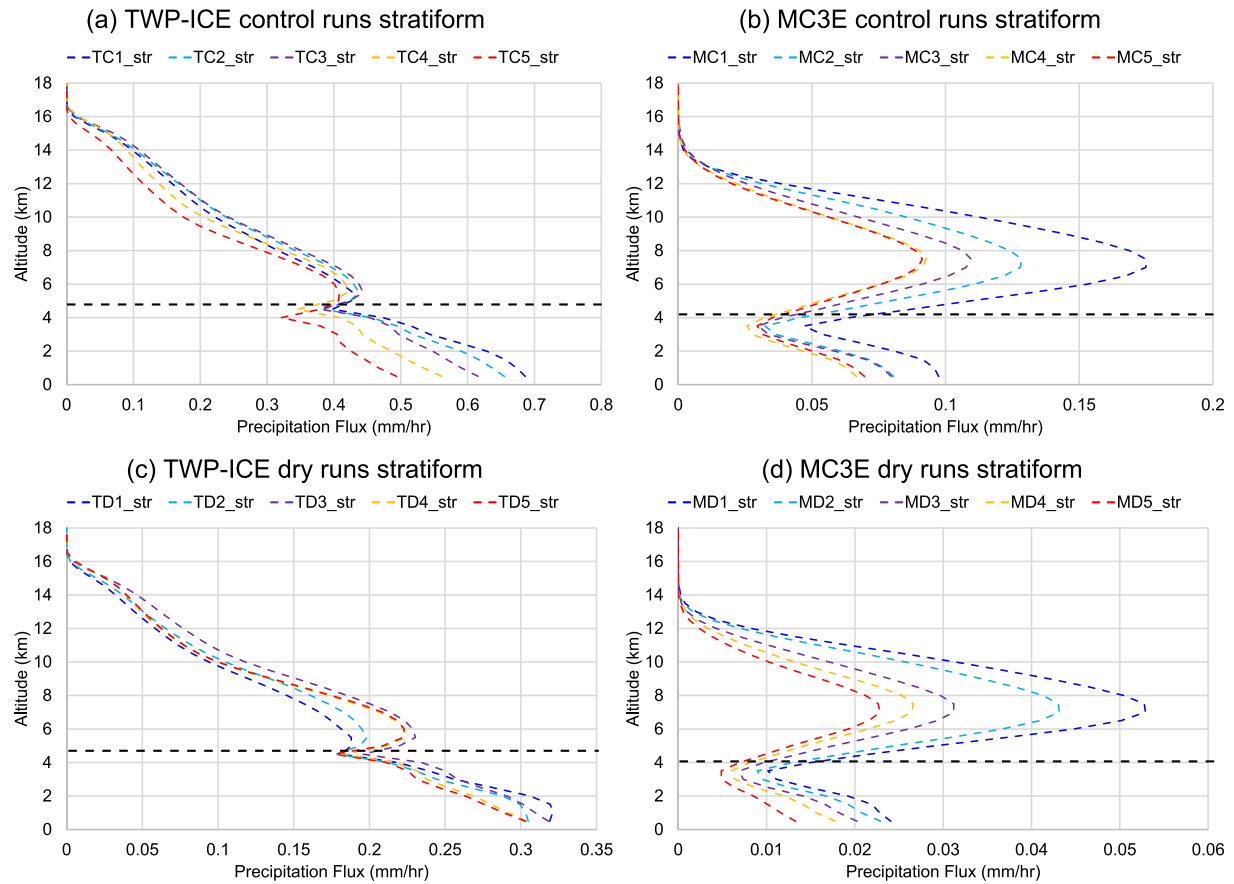


Figure 18. As in Figure 17 but for precipitation flux (mm hr^{-1}) in stratiform precipitation areas.

4.2. Competition Between Graupel and Hail Production

As described in section 2.2, hail particles are initiated through the following four pathways in the present model when the ambient temperature is below 0°C : (1) by snow particles with a bulk radius less than $\sim 550 \mu\text{m}$ and with rimed mass fractions over 95% consistent with bulk densities near 0.9 g cm^{-3} (rimed snow to hail), (2) through wet growth on graupel particles with diameters over a threshold determined according to environmental factors (Khain et al. 2011) (rimed graupel to hail), (3) when graupel particles achieve diameters $>10 \text{ mm}$ (giant graupel to hail), and (4) freezing of droplets with a bulk radius larger than $\sim 250 \mu\text{m}$ (frozen drop to hail). Once hail particles are initiated, the particle masses and sizes increase by accretion of supercooled water. On the other hand, graupel particles can be initiated if snow particles with a bulk radius exceeding $\sim 550 \mu\text{m}$ have a bulk density larger than 0.2 g cm^{-3} . This graupel initiation process through riming on snow is posterior to the process of rimed snow to hail because of the difference in the snow particle size ranges subjected to the transformation.

We conducted three types of additional simulations to check the various hail production processes. The SBM was modified as it excluded the processes of (a) rimed graupel to hail, (b) both rimed graupel to hail, and giant graupel to hail, and (c) frozen drop to hail. Figure 19 shows differences in hail mixing ratios in the three additional and baseline simulations. In summary, the two processes from graupel to hail is not prevalent in both cases, and the other two processes, i.e., rimed snow to hail and frozen drop to hail (particularly, in the MC3E) are predominant. The dominance of the frozen drop to hail process in the MC3E case is consistent with the dominant hailstone embryo type in Oklahoma in Knight (1981), in which frozen drop embryos in hailstones were much more frequent than graupel embryos.

Results in section 3.3.2 show that the increase in supercooled water with increasing CCN causes increase in hail in both the TWP-ICE and MC3E cases. This increase in hail is mainly contributed by the hail

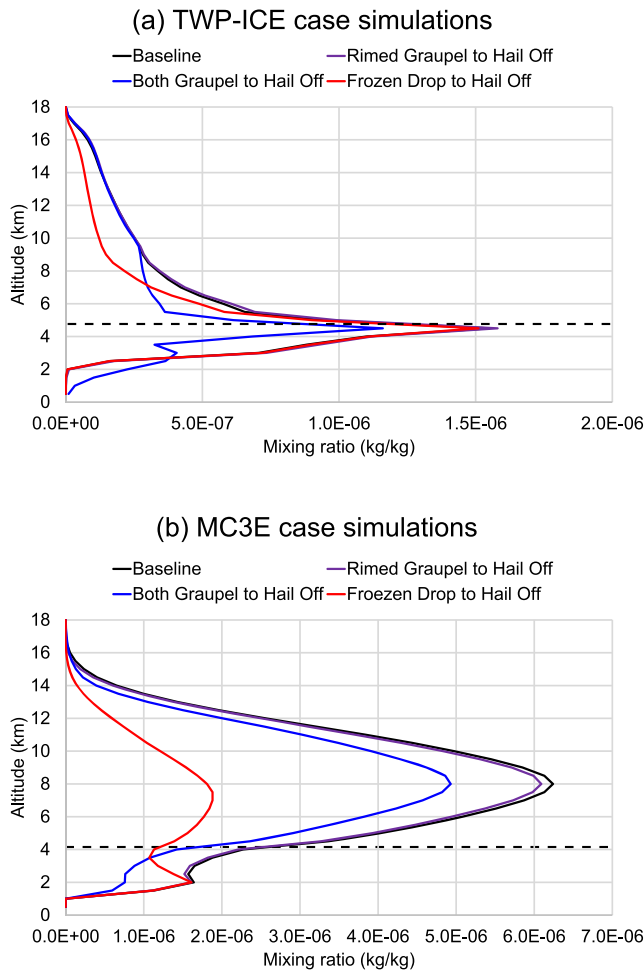


Figure 19. Vertical profiles of hail mixing ratio (kg kg^{-1}) averaged over the entire model domains for the last 18 hr of the simulation periods in (a) TWP-ICE and (b) MC3E cases. Black, purple, blue, and red lines denote the profiles in the baseline simulations (TC1 and MC5 in Table 1) and simulations excluding the change process of graupel to hail through wet growth, the change both through the wet growth and for graupel particles with the diameters over 10 mm, and the change of droplets with a bulk radius larger than $\sim 250 \mu\text{m}$ to hail by freezing, respectively. The black dashed lines denote approximate altitudes of 0°C isotherm.

comparison showed that the modeled CCN number concentrations near the surface agreed overall with the observations with maximum CCN number concentration error of roughly $1,000 \text{ cm}^{-3}$ over the MC3E simulation period. This value is less than the difference in near-surface CCN concentrations between the MC3E and TWP-ICE cases calculated from the downscaling. The latter comparison showed that the modeled aerosol concentrations were considerably lower than those of the airborne observations in the middle and upper troposphere. These discrepancies may be due to limitations in the aerosol reanalysis data set for downscaling and assumptions for prescribed aerosol PSD.

The results of the baseline simulation for each TWP-ICE and MC3E case were each compared with radar observations to overall confirm that the simulations captured contrasted characteristics in the maritime and continental deep convective systems, prior to investigating contrasted differences in the sensitivities to the aerosol and thermodynamics perturbations. The simulations contained errors in comparison to the observations such as differences in radar reflectivity spatial patterns, wider convective precipitation areas, higher precipitation rates, etc. However, both maritime observations and simulation showed similar characteristics that convective areas of irregular shapes and various sizes were surrounded by wide stratiform areas.

initialization through the processes of rimed snow and frozen drop to hail and subsequent increase by accretion of supercooled water. In the MC3E case, the increases in supercooled water with increasing CCN effectively shifts the supercooled water to hail rather than to graupel production. In the TWP-ICE case, however, hail production is considerably small via any of the four pathways as compared to production of snow and graupel, and graupel dominates the accretion of supercooled water. This distinction between the TWP-ICE and MC3E simulations is attributable to the difference in relative magnitudes and the peak altitudes of supercooled water and snow mixing ratios above the freezing level in convective precipitation regions (Figure S5). The conditionally averaged mixing ratios of cloud water and snow are similar at $\sim 6\text{--}8 \text{ km}$ height in convective regions in the MC3E simulations (Figure S5). Thus, supercooled water can generate large drops that quickly freeze to serve as hail embryos below the altitudes with significant snow. In contrast, in the TWP-ICE simulations, supercooled water is scavenged by abundant snow near the freezing level, so that supercooled water is used for production of graupel through riming of snow prior to satisfying the conditions for hail production. Furthermore, this difference in the TWP-ICE and MC3E simulations may be attributable to the difference in humidity in the middle troposphere and updraft strengths, which are related to snow and supercooled water amounts and their dominant altitudes above the freezing level.

5. Summary and Conclusions

A series of simulations were conducted to investigate the impact of CCN and CAPE on two different deep convective systems, one developed under maritime (TWP-ICE) and the other under continental (MC3E) environment. Aerosol perturbations were configured within the framework of dynamic aerosol downscaling from global aerosol reanalysis data. This approach enabled reasonable simulations to be performed wherein horizontal anomalies in the aerosol concentration fields were similar when perturbing the maritime and continental aerosol fields.

Aerosol number concentrations calculated from the downscaling were compared to those observed from a ground-based CCN particle counter and an airborne CPC in the MC3E case. The former compar-

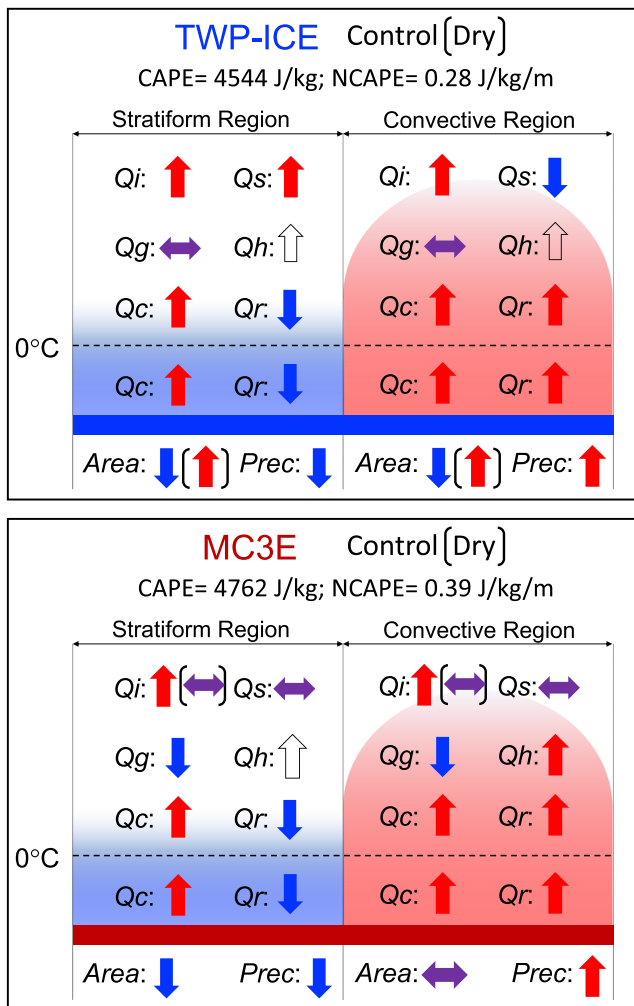


Figure 20. Schematic diagram summarizing the changes in various physical quantities to the increasing CCN concentration and the thermodynamics perturbations in the sensitivity experiments. The red upward (blue downward) arrows denote monotonic increase (decrease) in quantity with increasing modeled CCN concentrations; the white upward arrows show monotonic increase, but the mixing ratio is very small compared to others. The purple arrows mean nonmonotonic changes. The brackets denote results from the dry runs. The abbreviations correspond to the following physical quantities: *Area*: Area of convective or stratiform precipitation region; *Prec*: Surface precipitation rate of convective or stratiform precipitation region; *Qi*, *Qs*, *Qg*, *Qh*, *Qc*, and *Qr*: Mixing ratios of cloud ice, snow, graupel, hail, cloud water, and rain, respectively.

In contrast, the continental simulation reproduced overall characteristics of the observed system with clustered convective areas accompanied by stratiform areas.

Several physical quantities related to cloud and precipitation elements were intercompared in the sensitivity experiments to investigate their responses to the aerosol and/or thermodynamics perturbations. The results are schematically summarized in Figure 20. The effects on surface precipitation were similar overall for the TWP-ICE and MC3E cases and in the control and vapor reduced simulations. The precipitation from convective areas increased with increasing CCN concentrations, and its change had a more significant impact on the total precipitation than stratiform precipitation. The increase in CCN loading yielded the opposite impacts on the changes in the convective and stratiform precipitation areal coverages in the TWP-ICE control and vapor-reduced runs, while they were similar in the MC3E runs. The analysis on latent heat budgets, which could be tied to condensate budgets for precipitation, showed that the changes in the latent heating/cooling with the CCN concentration changes in our simulations were consistent with those for maritime and continental case simulations in previous studies (Khain, 2009).

Changes in supercooled water due to the CCN loading changes had different impacts on the cloud microphysics in the TWP-ICE and MC3E simulations. The increase in supercooled water with increasing CCN caused overall increases in graupel in the TWP-ICE simulations, whereas the reverse was true in the MC3E simulations. The increase in supercooled water enhanced the hail production in the MC3E simulations, which worked counter to the graupel production from snow through consumption of supercooled water. However, this process was not effective in TWP-ICE simulations, because supercooled water was scavenged by abundant snow near the freezing level and was used for production of graupel from snow. This distinction is attributable to the differences in relative magnitudes and the peak altitudes of supercooled water and snow amounts above the freezing level, and maybe also to the moisture and dynamics between the two cases.

This study showed complex and variable responses in the cloud and precipitation elements of specific maritime and continental deep convective systems to CCN and thermodynamic perturbations. However, it is still uncertain as to whether these findings are robust as the sensitivity experiments herein were configured only for a single maritime and a single continental case. Expanding the investigation to

other cases not limited to deep convection is a task for future study. For example, previous studies (e.g., Fan et al., 2007; Li et al., 2008) showed optimal aerosol concentration that maximized physical variables such as surface precipitation amounts; the optimal concentrations in these two previous studies were very high in the ranges they tested. Our simulation results did not show such optimal aerosol concentration and variables, rather most impacts in our simulations changed monotonically. A possible reason for this behavior is that the range of aerosol concentration tested in this study was limited to those between the two specific cases and did not include extremely polluted situations so that the simulations did not capture the optimal aerosol concentration which may be outside the range tested herein.

The simulation results, particularly the interplay between graupel and hail are likely largely dependent on the definitions of the hydrometeor particle categories and the mutual transformations designed in the

model microphysics. The model used in this study did not include more detailed initiation processes of hail and graupel particles (Iltoviz et al., 2016, 2018; Phillips et al., 2014, 2015). Including these processes may largely change the balance in graupel and hail production in response to aerosol and subsequent super-cooled water changes.

Data Availability Statement

The MC3E radar data are available in the Kinematic and hydrometer data products from scanning radars during MC3E (HKSR; <https://www.arm.gov/data/data-sources/hksr-117>). WRF-SBM simulation output files are available through NASA GSFC Cloud Library (<https://portal.nccs.nasa.gov/cloudlibrary/>) managed by NASA GSFC NCCS.

Acknowledgments

This work was funded by Department of Energy (DOE) Atmospheric System Research (ASR) program (Project managers: Shaima Nasiri and Ashley Williamson) in support of the project entitled, “Investigation of Hydrometeor Distributions in Continental and Maritime Storm Systems: Application of Cloud-Resolving Simulations, a Polarimetric Scanning Radar Simulator and Polarimetric Radar Observations” (DE-SC0014371). T. Iguchi, W.-K. Tao, T. Matsui, and S. Lang were also supported by the NASA Modeling, Analysis, and Prediction (MAP) Program. The computational resources were provided by two NASA High Performance Computing (HPC) facilities: NASA Center for Climate Simulation (NCCS) at Goddard Space Flight Center (GSFC) and NASA Advanced Supercomputing (NAS) Division at Ames Research Center. We wish to acknowledge the developers of the WRF-ARW and HUCM models in terms of their supports. We thank Stephen M. Saleeby of Colorado State University for helping us to get the data from the ARM aerosol observation system (AOS) CCN particle counter at the ARM SGP central facility site, and Ann M. Fridlind of NASA Goddard Institute for Space Studies (GISS) for providing the airborne CPC aerosol number concentration data obtained in the MC3E campaign. The authors thank the three anonymous reviewers and the journal Editors for their helpful comments in improving this paper.

References

Albrecht, B. A. (1989). Aerosols, cloud microphysics, and fractional cloudiness. *Science*, *245*(4923), 1227–1230. <https://doi.org/10.1126/science.245.4923.1227>

Andreae, M. O., Rosenfeld, D., Artaxo, P., Costa, A. A., Frank, G. P., Longo, K. M., & da Silva-Dias, M. A. F. (2004). Smoking rain clouds over the Amazon. *Science*, *303*, 1337–1342. <https://doi.org/10.1126/science.1092779>

Bell, T. L., Rosenfeld, D., Kim, K. M., Yoo, J. M., Lee, M. I., & Hahnberger, M. (2008). Midweek increase in US summer rain and storm heights suggests air pollution invigorates rainstorms. *Journal of Geophysical Research*, *113*, D02209. <https://doi.org/10.1029/2007JD008623>

Bosilovich, M. G., Akella, S., Coy, L., Cullather, R., Draper, C., Gelaro, R., et al. (2015). MERRA-2: Initial evaluation of the climate. In *Technical report series on global modeling and data assimilation volume 43*, NASA/TM-2015-104606/ (Vol. 43, pp. 1–139). Greenbelt, MD: National Aeronautics and Space Administration Goddard Space Flight Center. [Available online at <http://gmao.gsfc.nasa.gov/reanalysis/MERRA-2/docs/>]

Boyle, J., & Klein, S. A. (2010). Impact of horizontal resolution on climate model forecasts of tropical precipitation and diabatic heating for the TWP-ICE period. *Journal of Geophysical Research*, *115*, D23113. <https://doi.org/10.1029/2010JD014262>

Chin, M., Ginoux, P., Kinne, S., Torres, O., Holben, B. N., Duncan, B. N., et al. (2002). Tropospheric Aerosol Optical Thickness from the GOCART Model and Comparisons with Satellite and Sun Photometer Measurements. *Journal of the Atmospheric Sciences*, *59*(3), 461–483. [https://doi.org/10.1175/1520-0469\(2002\)059<0461:taoftf>2.0.co;2](https://doi.org/10.1175/1520-0469(2002)059<0461:taoftf>2.0.co;2)

Chin, M., Rood, R. B., Lin, S. J., Müller, J. F., & Thompson, A. M. (2000). Atmospheric sulfur cycle simulated in the global model GOCART: Model description and global properties. *Journal of Geophysical Research*, *105*, 24,671–24,687. <https://doi.org/10.1029/2000JD900384>

Chin, M., Savoie, D. L., Huebert, B. J., Bandy, A. R., Thornton, D. C., Bates, T. S., et al. (2000). Atmospheric sulfur cycle simulated in the global model GOCART: Comparison with field observations and regional budgets. *Journal of Geophysical Research*, *105*, 24,689–24,712. <https://doi.org/10.1029/2000JD900385>

Choi, I., Iguchi, T., Kim, S., Nakajima, T., & Yoon, S. (2014). The effect of aerosol representation on cloud microphysical properties in Northeast Asia. *Meteorology and Atmospheric Physics*, *123*(3-4), 181–194. <https://doi.org/10.1007/s00703-013-0288-y>

Chou, M.-D., & Suarez, M. J. (1999). *A solar radiation parameterization for atmospheric studies* (Vol. 15, pp. 1–51). Greenbelt, MD: National Aeronautics and Space Administration Goddard Space Flight Center.

Chou, M.-D., Suarez, M. J., Liang, X.-Z., & Yan, M. M. H., (2001). *A thermal infrared radiation parameterization for atmospheric studies*, 19, 1–68. Greenbelt, MD: National Aeronautics and Space Administration Goddard Space Flight Center.

da Silva, A. M., Randles, C. A., Buchard, V., Darmenov, A., Colarco, P. R., & Govindaraju, R. (2015). File Specification for the MERRA Aerosol Reanalysis (MERRAero). In *GMAO Office Note No. 7 (Version 1.0)* (pp. 1–30). Greenbelt, MD: National Aeronautics and Space Administration Goddard Space Flight Center. Retrieved from http://gmao.gsfc.nasa.gov/pubs/office_notes

Dee, D. P., Uppala, S. M., Simmons, A. J., Berrisford, P., Poli, P., Kobayashi, S., et al. (2011). The ERA-Interim reanalysis: Configuration and performance of the data assimilation system. *Quarterly Journal of the Royal Meteorological Society*, *137*(656), 553–597. <https://doi.org/10.1002/qj.828>

Dennis, A. S., & Musil, D. J. (1973). Calculations of hailstone growth and trajectories in a simple cloud model. *Journal of the Atmospheric Sciences*, *30*(2), 278–288. [https://doi.org/10.1175/1520-0469\(1973\)030<0278:COHGAT>2.0.CO;2](https://doi.org/10.1175/1520-0469(1973)030<0278:COHGAT>2.0.CO;2)

Dolan, B., Rutledge, S. A., Lim, S., Chandrasekar, V., & Thurai, M. (2013). A robust C-band hydrometeor identification algorithm and application to a long-term polarimetric radar dataset. *Journal of Applied Meteorology and Climatology*, *52*(9), 2162–2186. <https://doi.org/10.1175/JAMC-D-12-0275.1>

Fan, J., Han, B., Varble, A., Morrison, H., North, K., Kollias, P., et al. (2017). Cloud-resolving model intercomparison of an MC3E squall line case: Part I—Convective updrafts. *Journal of Geophysical Research: Atmospheres*, *122*, 9351–9378. <https://doi.org/10.1002/2017JD026622>

Fan, J., Leung, L. R., Li, Z., Morrison, H., Chen, H., Zhou, Y., et al. (2012). Aerosol impacts on clouds and precipitation in eastern China: Results from bin and bulk microphysics. *Journal of Geophysical Research*, *117*, D00K36. <https://doi.org/10.1029/2011JD016537>

Fan, J., Leung, L. R., Rosenfeld, D., Chen, Q., Li, Z., Zhang, J., & Yan, H. (2013). Microphysical effects determine macrophysical response for aerosol impacts on deep convective clouds. *Proceedings of the National Academy of Sciences*, *110*, E4581–E4590. <https://doi.org/10.1073/pnas.1316830110>

Fan, J., Liu, Y.-C., Xu, K.-M., North, K., Collis, S., Dong, X., et al. (2015). Improving representation of convective transport for scale-aware parameterization: 1. Convection and cloud properties simulated with spectral bin and bulk microphysics. *Journal of Geophysical Research: Atmospheres*, *120*, 3485–3509. <https://doi.org/10.1002/2014JD022142>

Fan, J., Rosenfeld, D., Ding, Y., Leung, L. R., & Li, Z. (2012). Potential aerosol indirect effects on atmospheric circulation and radiative forcing through deep convection. *Geophysical Research Letters*, *39*, L09806. <https://doi.org/10.1029/2012GL051851>

Fan, J., Rosenfeld, D., Zhang, Y., Giangrande, S. E., Li, Z., Machado, L. A. T., et al. (2018). Substantial convection and precipitation enhancements by ultrafine aerosol particles. *Science*, *359*(6374), 411–418. <https://doi.org/10.1126/science.aan8461>

Fan, J., Yuan, T., Comstock, J. M., Ghan, S., Khain, A., Leung, L. R., et al. (2009). Dominant role by vertical wind shear in regulating aerosol effects on deep convective clouds. *Journal of Geophysical Research*, *114*, D22206. <https://doi.org/10.1029/2009JD012352>

- Fan, J., Zhang, R., Li, G., & Tao W.-K. (2007). Effects of aerosols and relative humidity on cumulus clouds. *Journal of Geophysical Research*, *112*, D14204. <https://doi.org/10.1029/2006JD008136>
- Fridlind, A. M., Ackerman, A. S., Chaboureau, J. P., Fan, J., Grabowski, W. W., Hill, A. A., et al. (2012). A comparison of TWP-ICE observational data with cloud-resolving model results. *Journal of Geophysical Research*, *117*, D05204. <https://doi.org/10.1029/2011JD016595>
- Gao, W., Fan, J., Easter, R. C., Yang, Q., Zhao, C., & Ghan, S. J. (2016). Coupling spectral-bin cloud microphysics with the MOSAIC aerosol model in WRF-Chem: Methodology and results for marine stratocumulus clouds. *Journal of Advances in Modeling Earth Systems*, *8*(3), 1289–1309. <https://doi.org/10.1002/2016MS000676>
- Ghan, S., Laulainen, N., Easter, R., Wagoner, R., Nemesure, S., Chapman, E., et al. (2001). Evaluation of aerosol direct radiative forcing in MIRAGE. *Journal of Geophysical Research*, *106*(D6), 5295–5316. <https://doi.org/10.1029/2000JD900502>
- Grabowski, W. W. (2015). Untangling microphysical impacts on deep convection applying a novel modeling methodology. *Journal of the Atmospheric Sciences*, *72*(6), 2446–2464. <https://doi.org/10.1175/JAS-D-14-0307.1>
- Grabowski, W. W. (2018). Can the impact of aerosols on deep convection be isolated from meteorological effects in atmospheric observations? *Journal of the Atmospheric Sciences*, *75*(10), 3347–3363. <https://doi.org/10.1175/JAS-D-18-0105.1>
- Grant, L. D., & van den Heever, S. C. (2015). Cold pool and precipitation responses to aerosol loading: Modulation by dry layers. *Journal of the Atmospheric Sciences*, *72*(4), 1398–1408. <https://doi.org/10.1175/JAS-D-14-0260.1>
- Grell, G. A., & Freitas, S. R. (2014). A scale and aerosol aware stochastic convective parameterization for weather and air quality modeling. *Atmospheric Chemistry and Physics*, *14*(10), 5233–5250. <https://doi.org/10.5194/acp-14-5233-2014>
- Hegg, D. A., Radke, L. F., & Hobbs, P. V. (1991). Measurements of Aitken nuclei and cloud condensation nuclei in the marine atmosphere and their relation to the DMS-cloud-climate hypothesis. *Journal of Geophysical Research*, *96*(D10), 18,727–18,733. <https://doi.org/10.1029/91JD01870>
- Hudson, J. G., & Yum, S. S. (2001). Maritime–continental drizzle contrasts in small cumuli. *Journal of the Atmospheric Sciences*, *58*(8), 915–926. [https://doi.org/10.1175/1520-0469\(2001\)058<0915:MCDCIS>2.0.CO;2](https://doi.org/10.1175/1520-0469(2001)058<0915:MCDCIS>2.0.CO;2)
- Igel, A. L., Van Den Heever, S. C., Naud, C. M., Saleeby, S. M., & Posselt, D. J. (2013). Sensitivity of warm-frontal processes to cloud-nucleating aerosol concentrations. *Journal of the Atmospheric Sciences*, *70*(6), 1768–1783. <https://doi.org/10.1175/JAS-D-12-0170.1>
- Iguchi, T., Choi, I.-J., Sato, Y., Suzuki, K., & Nakajima, T. (2015). Overview of the development of the aerosol loading interface for cloud microphysics in simulation (ALICIS). *Progress in Earth and Planetary Science*, *2*, 1–23. <https://doi.org/10.1186/s40645-015-0075-0>
- Iguchi, T., Matsui, T., Shi, J. J., Tao, W.-K., Khain, A. P., Hou, A., et al. (2012). Numerical analysis using WRF-SBM for the cloud microphysical structures in the C3VP field campaign: Impacts of supercooled droplets and resultant riming on snow microphysics. *Journal of Geophysical Research*, *117*, D23206. <https://doi.org/10.1029/2012JD018101>
- Iguchi, T., Matsui, T., Tao, W.-K., Khain, A. P., Phillips, V. T. J., Kidd, C., et al. (2014). WRF-SBM simulations of melting-layer structure in mixed-phase precipitation events observed during LPVEx. *Journal of Applied Meteorology and Climatology*, *53*(12), 2710–2731. <https://doi.org/10.1175/JAMC-D-13-0334.1>
- Iguchi, T., Nakajima, T., Khain, A., Saito, K., Takemura, T., & Suzuki, K. (2008). Modeling the influence of aerosols on cloud microphysical properties in the east Asia region using a mesoscale model coupled with a bin-based cloud microphysics scheme. *Journal of Geophysical Research*, *113*, D14215. <https://doi.org/10.1029/2007JD009774>
- Ilotoviz, E., Khain, A., Ryzhkov, A. V., & Snyder, J. C. (2018). Relationship between aerosols, hail microphysics, and Z DR columns. *Journal of the Atmospheric Sciences*, *75*(6), 1755–1781. <https://doi.org/10.1175/JAS-D-17-0127.1>
- Ilotoviz, E., Khain, A. P., Benmoshe, N., Phillips, V. T. J., & Ryzhkov, A. V. (2016). Effect of aerosols on freezing drops, hail, and precipitation in a midlatitude storm. *Journal of the Atmospheric Sciences*, *73*(1), 109–144. <https://doi.org/10.1175/JAS-D-14-0155.1>
- Janjic, Z. I. (1994). The step-mountain eta coordinate model: Further developments of the convection, viscous sublayer, and turbulence closure schemes. *Monthly Weather Review*, *122*(5), 927–945. [https://doi.org/10.1175/1520-0493\(1994\)122<0927:TSMECM>2.0.CO;2](https://doi.org/10.1175/1520-0493(1994)122<0927:TSMECM>2.0.CO;2)
- Jensen, M. P., Kollias, P., & Giangrande, S. (2016). The midlatitude continental convective clouds experiment (MC3E). *Bulletin of the American Meteorological Society*, *97*(9), 1667–1686. <https://doi.org/10.1175/BAMS-D-14-00228.1>
- Jeon, Y.-L., Moon, S., Lee, H., Baik, J.-J., & Lkhamjav, J. (2018). Non-monotonic dependencies of cloud microphysics and precipitation on aerosol loading in deep convective clouds: A case study using the WRF model with bin microphysics. *Atmosphere*, *9*(11), 434. <https://doi.org/10.3390/atmos9110434>
- Jouan, C., & Milbrandt, J. A. (2019). The importance of the ice-phase microphysics parameterization for simulating the effects of changes to CCN concentrations in deep convection. *Journal of the Atmospheric Sciences*, *76*(6), 1727–1752. <https://doi.org/10.1175/JAS-D-18-0168.1>
- Kalina, E. A., Friedrich, K., Morrison, H., & Bryan, G. H. (2014). Aerosol effects on idealized supercell thunderstorms in different environments. *Journal of the Atmospheric Sciences*, *71*(12), 4558–4580. <https://doi.org/10.1175/JAS-D-14-0037.1>
- Khain, A., & Lynn, B. (2009). Simulation of a supercell storm in clean and dirty atmosphere using weather research and forecast model with spectral bin microphysics. *Journal of Geophysical Research*, *114*, D19209. <https://doi.org/10.1029/2009JD011827>
- Khain, A., Lynn, B., & Dudhia, J. (2010). Aerosol effects on intensity of landfalling hurricanes as seen from simulations with the WRF model with spectral bin microphysics. *Journal of the Atmospheric Sciences*, *67*(2), 365–384. <https://doi.org/10.1175/2009JAS3210.1>
- Khain, A., & Pokrovsky, A. (2004). Simulation of Effects of Atmospheric Aerosols on Deep Turbulent Convective Clouds Using a Spectral Microphysics Mixed-Phase Cumulus Cloud Model. Part II: Sensitivity Study. *Journal of the Atmospheric Sciences*, *61*(24), 2983–3001. <https://doi.org/10.1175/jas-3281.1>
- Khain, A., Pokrovsky, A., Pinsky, M., Seifert, A., & Phillips, V. (2004). Simulation of effects of atmospheric aerosols on deep turbulent convective clouds using a spectral microphysics mixed-phase cumulus cloud model Part I: Model description and possible applications. *Journal of the Atmospheric Sciences*, *61*, 2963–2982. <https://doi.org/10.1175/jas-3350.1>
- Khain, A., Pokrovsky, A., & Sednev, I. (1999). Some effects of cloud–aerosol interaction on cloud microphysics structure and precipitation formation: Numerical experiments with a spectral microphysics cloud ensemble model. *Atmospheric Research*, *52*(3), 195–220. [https://doi.org/10.1016/S0169-8095\(99\)00027-7](https://doi.org/10.1016/S0169-8095(99)00027-7)
- Khain, A., Rosenfeld, D., & Pokrovsky, A. (2005). Aerosol impact on the dynamics and microphysics of deep convective clouds. *Quarterly Journal of the Royal Meteorological Society: A Journal of the Atmospheric Sciences, Applied Meteorology and Physical Oceanography*, *131*(611), 2639–2663. <https://doi.org/10.1256/qj.04.62>
- Khain, A., Rosenfeld, D., Pokrovsky, A., Blahak, U., & Ryzhkov, A. (2011). The role of CCN in precipitation and hail in a mid-latitude storm as seen in simulations using a spectral (bin) microphysics model in a 2D dynamic frame. *Atmospheric Research*, *99*(1), 129–146. <https://doi.org/10.1016/j.atmosres.2010.09.015>

- Khain, A. P. (2009). Notes on state-of-the-art investigations of aerosol effects on precipitation: A critical review. *Environmental Research Letters*, 4(1), 015004. <https://doi.org/10.1088/1748-9326/4/1/015004>
- Khain, A. P., Beheng, K. D., Heymsfield, A., Korolev, A., Krichak, S. O., Levin, Z., et al. (2015). Representation of microphysical processes in cloud-resolving models: Spectral (bin) microphysics versus bulk parameterization. *Reviews of Geophysics*, 53(2), 247–322. <https://doi.org/10.1002/2014RG000468>
- Khain, A. P., BenMoshe, N., & Pokrovsky, A. (2008). Factors determining the impact of aerosols on surface precipitation from clouds: An attempt at classification. *Journal of the Atmospheric Sciences*, 65(6), 1721–1748. <https://doi.org/10.1175/2007JAS2515.1>
- Khain, A. P., Leung, L. R., Lynn, B., & Ghan, S. (2009). Effects of aerosols on the dynamics and microphysics of squall lines simulated by spectral bin and bulk parameterization schemes. *Journal of Geophysical Research*, 114, D22203. <https://doi.org/10.1029/2009JD011902>
- Khain, A. P., Phillips, V., Benmoshe, N., & Pokrovsky, A. (2012). The role of small soluble aerosols in the microphysics of deep maritime clouds. *Journal of the Atmospheric Sciences*, 69(9), 2787–2807. <https://doi.org/10.1175/2011JAS3649.1>
- Khain, A. P., & Pinsky, M. (2018). *Physical processes in clouds and cloud modeling*. University Printing House Shaftesbury Road Cambridge CB2 8BS United Kingdom. Cambridge, UK: Cambridge University Press.
- Knight, N. C. (1981). The climatology of hailstone embryos. *Journal of Applied Meteorology*, 20(7), 750–755. [https://doi.org/10.1175/1520-0450\(1981\)020<0750:TCOHE>2.0.CO;2](https://doi.org/10.1175/1520-0450(1981)020<0750:TCOHE>2.0.CO;2)
- Köhler, H. (1936). The nucleus in and the growth of hygroscopic droplets. *Transactions of the Faraday Society*, 32(0), 1152–1161. <https://doi.org/10.1039/TF9363201152>
- Krueger, S. K., Morrison, H., & Fridlind, A. M. (2016). Cloud-resolving modeling: ARM and the GCSS story. *Meteorological Monographs*, 57, 25–21. <https://doi.org/10.1175/amsmonographs-d-15-0047.1>
- Lang, S. E., Tao, W.-K., Chern, J.-D., Wu, D., & Li, X. (2014). Benefits of a fourth ice class in the simulated radar reflectivities of convective systems using a bulk microphysics scheme. *Journal of the Atmospheric Sciences*, 71(10), 3583–3612. <https://doi.org/10.1175/JAS-D-13-0330.1>
- Lebo, Z. J., & Morrison, H. (2014). Dynamical effects of aerosol perturbations on simulated idealized squall lines. *Monthly Weather Review*, 142(3), 991–1009. <https://doi.org/10.1175/MWR-D-13-00156.1>
- Lebo, Z. J., & Seinfeld, J. H. (2011). Theoretical basis for convective invigoration due to increased aerosol concentration. *Atmospheric Chemistry and Physics*, 11(11), 5407–5429. <https://doi.org/10.5194/acp-11-5407-2011>
- Lee, S. S. (2017). Interactions between aerosol absorption, thermodynamics, dynamics, and microphysics and their impacts on a multiple-cloud system. *Climate Dynamics*, 49(11–12), 3905–3921. <https://doi.org/10.1007/s00382-017-3552-x>
- Lee, S. S., Donner, L. J., & Phillips, V. T. J. (2009). Impacts of aerosol chemical composition on microphysics and precipitation in deep convection. *Atmospheric Research*, 94(2), 220–237. <https://doi.org/10.1016/j.atmosres.2009.05.015>
- Lee, S. S., Donner, L. J., Phillips, V. T. J., & Ming, Y. (2008a). Examination of aerosol effects on precipitation in deep convective clouds during the 1997 ARM summer experiment. *Quarterly Journal of the Royal Meteorological Society*, 134(634), 1201–1220. <https://doi.org/10.1002/qj.287>
- Lee, S. S., Donner, L. J., Phillips, V. T. J., & Ming, Y. (2008b). The dependence of aerosol effects on clouds and precipitation on cloud-system organization, shear and stability. *Journal of Geophysical Research*, 113, D16202. <https://doi.org/10.1029/2007JD009224>
- Levin, Z., & Cotton, W. R. (2008). *Aerosol pollution impact on precipitation: A scientific review*. New York, NY: Springer Science & Business Media.
- Li, G., Wang, Y., Lee, K. H., Diao, Y., & Zhang, R. (2009). Impacts of aerosols on the development and precipitation of a mesoscale squall line. *Journal of Geophysical Research*, 114, D17205. <https://doi.org/10.1029/2008JD011581>
- Li, G., Wang, Y., & Zhang, R. (2008). Implementation of a two-moment bulk microphysics scheme to the WRF model to investigate aerosol-cloud interaction. *Journal of Geophysical Research*, 113, D15211. <https://doi.org/10.1029/2007jd009361>
- Li, Z., Niu, F., Fan, J., Liu, Y., Rosenfeld, D., & Ding, Y. (2011). Long-term impacts of aerosols on the vertical development of clouds and precipitation. *Nature Geoscience*, 4(12), 888–894. <https://doi.org/10.1038/ngeo1313>
- Loftus, A. M., & Cotton, W. R. (2014). Examination of CCN impacts on hail in a simulated supercell storm with triple-moment hail bulk microphysics. *Atmospheric Research*, 147, 183–204. <https://doi.org/10.1016/j.atmosres.2014.04.017>
- Lucas, C., Zipser, E. J., & LeMone, M. A. (1994a). Convective available potential energy in the environment of oceanic and continental clouds: Correction and comments. *Journal of the Atmospheric Sciences*, 51(24), 3829–3830. [https://doi.org/10.1175/1520-0469\(1994\)051<3829:CAPEIT>2.0.CO;2](https://doi.org/10.1175/1520-0469(1994)051<3829:CAPEIT>2.0.CO;2)
- Lucas, C., Zipser, E. J., & Lemone, M. A. (1994b). Vertical velocity in oceanic convection off tropical Australia. *Journal of the Atmospheric Sciences*, 51(21), 3183–3193. [https://doi.org/10.1175/1520-0469\(1994\)051<3183:VVIOCO>2.0.CO;2](https://doi.org/10.1175/1520-0469(1994)051<3183:VVIOCO>2.0.CO;2)
- Lynn, B. H., Khain, A. P., Dudhia, J., Rosenfeld, D., Pokrovsky, A., & Seifert, A. (2005a). Spectral (bin) microphysics coupled with a mesoscale model (MM5). Part I: Model description and first results. *Monthly Weather Review*, 133, 44–58. <https://doi.org/10.1175/mwr-2840.1>
- Lynn, B. H., Khain, A. P., Dudhia, J., Rosenfeld, D., Pokrovsky, A., & Seifert, A. (2005b). Spectral (bin) microphysics coupled with a mesoscale model (MM5). Part II: Simulation of a CaPE rain event with a squall line. *Monthly Weather Review*, 133(1), 59–71. <https://doi.org/10.1175/MWR-2841.1>
- Marinescu, P. J., Heever, S. C., Saleeby, S. M., & Kreidenweis, S. M. (2016). The microphysical contributions to and evolution of latent heating profiles in two MC3E MCSs. *Journal of Geophysical Research: Atmospheres*, 121, 7913–7935. <https://doi.org/10.1002/2016JD024762>
- Masunaga, H., & Kummerow, C. D. (2005). Combined radar and radiometer analysis of precipitation profiles for a parametric retrieval algorithm. *Journal of Atmospheric and Oceanic Technology*, 22(7), 909–929. <https://doi.org/10.1175/JTECH1751.1>
- Matsui, T., Chern, J.-D., Tao, W.-K., Lang, S., Satoh, M., Hashino, T., & Kubota, T. (2016). On the land–ocean contrast of tropical convection and microphysics statistics derived from TRMM satellite signals and global storm-resolving models. *Journal of Hydrometeorology*, 17(5), 1425–1445. <https://doi.org/10.1175/JHM-D-15-0111.1>
- Matsui, T., Dolan, B., Rutledge, S. A., Tao, W.-K., Iguchi, T., Barnum, J., & Lang, S. (2019). POLARRIS: A polarimetric radar retrieval and instrument simulator. *Journal of Geophysical Research: Atmospheres*, 124, 4634–4657. <https://doi.org/10.1029/2018JD028317>
- Matsui, T., Iguchi, T., Li, X., Han, M., Tao, W.-K., Petersen, W., et al. (2013). GPM satellite simulator over ground validation sites. *Bulletin of the American Meteorological Society*, 94(11), 1653–1660. <https://doi.org/10.1175/BAMS-D-12-00160.1>
- May, P. T., Mather, J. H., Vaughan, G., Jakob, C., McFarquhar, G. M., Bower, K. N., & Mace, G. G. (2008). The tropical warm pool international cloud experiment. *Bulletin of the American Meteorological Society*, 89(5), 629–646. <https://doi.org/10.1175/BAMS-89-5-629>

- Mitra, S. K., Vohl, O., Ahr, M., & Pruppacher, H. R. (1990). A wind tunnel and theoretical study of the melting behavior of atmospheric ice particles IV: Experiment and theory for snow flakes. *Journal of the Atmospheric Sciences*, *47*, 584–591. [https://doi.org/10.1175/1520-0469\(1990\)047<0584:awtats>2.0.co;2](https://doi.org/10.1175/1520-0469(1990)047<0584:awtats>2.0.co;2)
- Mohr, C. G., & Miller, L. J. (1983). CEDRIC—A software package for Cartesian space editing, synthesis, and display of radar fields under interactive control. In *Preprints, 21st Conf. On Radar Meteorology*, (pp. 559–574). Edmonton, AB, Canada, Amer.: Meteor. Soc.
- Molod, A., Takacs, L., Suarez, M., & Bacmeister, J. (2015). Development of the GEOS-5 atmospheric general circulation model: Evolution from MERRA to MERRA2. *Geoscientific Model Development*, *8*(5), 1339–1356. <https://doi.org/10.5194/gmd-8-1339-2015>
- Morrison, H. (2012). On the robustness of aerosol effects on an idealized supercell storm simulated with a cloud system-resolving model. *Atmospheric Chemistry and Physics*, *12*(16), 7689–7705. <https://doi.org/10.5194/acp-12-7689-2012>
- Morrison, H., & Grabowski, W. W. (2011). Cloud-system resolving model simulations of aerosol indirect effects on tropical deep convection and its thermodynamic environment. *Atmospheric Chemistry and Physics*, *11*(20), 10,503–10,523. <https://doi.org/10.5194/acp-11-10503-2011>
- Morrison, H., Thompson, G., & Tatarskii, V. (2009). Impact of cloud microphysics on the development of trailing stratiform precipitation in a simulated squall line: Comparison of one-and two-moment schemes. *Monthly Weather Review*, *137*(3), 991–1007. <https://doi.org/10.1175/2008MWR2556.1>
- Mrowiec, A. A., Rio, C., Fridlind, A. M., Ackerman, A. S., Del Genio, A. D., Pauluis, O. M., et al. (2012). Analysis of cloud-resolving simulations of a tropical mesoscale convective system observed during TWP-ICE: Vertical Fluxes and draft properties in convective and stratiform regions. *Journal of Geophysical Research*, *117*, D19201. <https://doi.org/10.1029/2012JD017759>
- National Centers for Environmental Prediction/National Weather Service/NOAA/U.S. Department of Commerce (2000). *NCEP FNL operational model global tropospheric analyses, continuing from July 1999*. Boulder, CO. Research Data Archive at the National Center for Atmospheric Research, Computational and Information Systems Laboratory. [Available online at <https://doi.org/10.5065/D6M043C6>.]
- Noppel, H., Blahak, U., Seifert, A., & Beheng, K. D. (2010). Simulations of a hailstorm and the impact of CCN using an advanced two-moment cloud microphysical scheme. *Atmospheric Research*, *96*(2-3), 286–301. <https://doi.org/10.1016/j.atmosres.2009.09.008>
- Petch, J., Hill, A., Davies, L., Fridlind, A., Jakob, C., Lin, Y., et al. (2014). Evaluation of intercomparisons of four different types of model simulating TWP-ICE. *Quarterly Journal of the Royal Meteorological Society*, *140*(680), 826–837. <https://doi.org/10.1002/qj.2192>
- Peters-Lidard, C. D., Kemp, E. M., Matsui, T., Santanello, J. A., Kumar, S. V., Jacob, J. P., et al. (2015). Integrated modeling of aerosol, cloud, precipitation and land processes at satellite-resolved scales. *Environmental Modelling & Software*, *67*, 149–159. <https://doi.org/10.1016/j.envsoft.2015.01.007>
- Phillips, V. T. J., Choullarton, T. W., Blyth, A. M., & Latham, J. (2002). The influence of aerosol concentrations on the glaciation and precipitation of a cumulus cloud. *Quarterly Journal of the Royal Meteorological Society*, *128*(581), 951–971. <https://doi.org/10.1256/0035900021643601>
- Phillips, V. T. J., Khain, A., Benmoshe, N., & Iltoviz, E. (2014). Theory of time-dependent freezing Part I: Description of scheme for wet growth of hail. *Journal of the Atmospheric Sciences*, *71*, 4527–4557.
- Phillips, V. T. J., Khain, A., Benmoshe, N., Iltoviz, E., & Ryzhkov, A. (2015). Theory of time-dependent freezing Part II: Scheme for freezing raindrops and simulations by a cloud model with spectral bin microphysics. *Journal of the Atmospheric Sciences*, *72*, 262–286. <https://doi.org/10.1175/jas-d-13-0376.1>
- Phillips, V. T. J., Pokrovsky, A., & Khain, A. (2007). The influence of time-dependent melting on the dynamics and precipitation production in maritime and continental storm clouds. *Journal of the Atmospheric Sciences*, *64*(2), 338–359. <https://doi.org/10.1175/JAS3832.1>
- Pruppacher, H. R., & Klett, J. D. (1997). *Microphysics of Clouds and Precipitation* (2nd ed., pp. 1–914). New York, NY: Oxford University Press.
- Pu, Z., & Lin, C. (2015). Evaluation of double-moment representation of ice hydrometeors in bulk microphysical parameterization: Comparison between WRF numerical simulations and UND-citation data during MC3E. *Geoscience Letters*, *2*(1), 11. <https://doi.org/10.1186/s40562-015-0028-x>
- Radke, L. F., Coakley, J. A., & King, M. D. (1989). Direct and remote sensing observations of the effects of ships on clouds. *Science*, *246*(4934), 1146–1149. <https://doi.org/10.1126/science.246.4934.1146>
- Randles, C. A., da Silva, A. M., Buchard, V., Colarco, P. R., Darmenov, A., Govindaraju, R., et al. (2017). The MERRA-2 aerosol reanalysis, 1980 onward Part I: System description and data assimilation evaluation. *Journal of Climate*, *30*(17), 6823–6850. <https://doi.org/10.1175/JCLI-D-16-0609.1>
- Rasmussen, R. M., & Heymsfield, A. J. (1987). Melting and shedding of graupel and hail Part I: Model physics. *Journal of the Atmospheric Sciences*, *44*, 2754–2763. [https://doi.org/10.1175/1520-0469\(1987\)044<2754:masoga>2.0.co;2](https://doi.org/10.1175/1520-0469(1987)044<2754:masoga>2.0.co;2)
- Rosenfeld, D., & Lensky, I. M. (1998). Satellite-based insights into precipitation formation processes in continental and maritime convective clouds. *Bulletin of the American Meteorological Society*, *79*(11), 2457–2476. [https://doi.org/10.1175/1520-0477\(1998\)079<2457:SBIIPF>2.0.CO;2](https://doi.org/10.1175/1520-0477(1998)079<2457:SBIIPF>2.0.CO;2)
- Rosenfeld, D., Lohmann, U., Raga, G. B., O'Dowd, C. D., Kulmala, M., Fuzzi, S., et al. (2008). Flood or drought: How do aerosols affect precipitation? *Science*, *321*(5894), 1309–1313. <https://doi.org/10.1126/science.1160606>
- Rotunno, R., Klemp, J. B., & Weisman, M. L. (1988). A theory for strong, long-lived squall lines. *Journal of the Atmospheric Sciences*, *45*(3), 463–485. [https://doi.org/10.1175/1520-0469\(1988\)045<0463:ATFSSL>2.0.CO;2](https://doi.org/10.1175/1520-0469(1988)045<0463:ATFSSL>2.0.CO;2)
- Saleeby, S. M., van den Heever, S. C., Marinescu, P. J., Kreidenweis, S. M., & DeMott, P. J. (2016). Aerosol effects on the anvil characteristics of mesoscale convective systems. *Journal of Geophysical Research: Atmospheres*, *121*, 10–880. <https://doi.org/10.1002/2016JD025082>
- Seifert, A., & Beheng, K. D. (2006). A two-moment cloud microphysics parameterization for mixed-phase clouds. Part 2: Maritime vs. continental deep convective storms. *Meteorology and Atmospheric Physics*, *92*(1-2), 67–82. <https://doi.org/10.1007/s00703-005-0113-3>
- Seifert, A., Khain, A., Pokrovsky, A., & Beheng, K. D. (2006). A comparison of spectral bin and two-moment bulk mixed-phase cloud microphysics. *Atmospheric Research*, *80*(1), 46–66. <https://doi.org/10.1016/j.atmosres.2005.06.009>
- Skamarock, W. C. (2004). Evaluating mesoscale NWP models using kinetic energy spectra. *Monthly Weather Review*, *132*(12), 3019–3032. <https://doi.org/10.1175/MWR2830.1>
- Skamarock, W. C., Klemp, J. B., Dudhin, J., Gill, D. O., Barker, D. M., Duda, M. G., et al. (2008). *A description of the advanced research WRF version 3*. NCAR Tech. Note NCAR/TN-4751STR (p. 113). Boulder, CO: University Corporation for Atmospheric Research. <https://doi.org/10.5065/D68S4MVH>
- Squires, P. (1956). The microstructure of cumuli in maritime and continental air. *Tellus*, *8*, 443–444. <https://doi.org/10.3402/tellusa.v8i4.9040>
- Squires, P. (1958). The microstructure and colloidal stability of warm clouds: Part II—The causes of the variations in microstructure. *Tellus*, *10*, 262–271. <https://doi.org/10.3402/tellusa.v10i2.9228>

- Squires, P., & Twomey, S. (1960). The relation between cloud droplet spectra and the spectrum of cloud nuclei. In W. E. Smith & H. Weickmann (Eds.), *Physics of precipitation: proceedings of the cloud physics conference, Geophysical Monograph Series* (Vol. 5, pp. 211–219). Washington, DC: American Geophysical Union.
- Steiner, M., Houze, R. A. Jr., & Yuter, S. E. (1995). Climatological characterization of three-dimensional storm structure from operational radar and rain gauge data. *Journal of Applied Meteorology*, 34(9), 1978–2007. [https://doi.org/10.1175/1520-0450\(1995\)034<1978:CCOTDS>2.0.CO;2](https://doi.org/10.1175/1520-0450(1995)034<1978:CCOTDS>2.0.CO;2)
- Stolz, D. C., Rutledge, S. A., & Pierce, J. R. (2015). Simultaneous influences of thermodynamics and aerosols on deep convection and lightning in the tropics. *Journal of Geophysical Research: Atmospheres*, 120, 6207–6231. <https://doi.org/10.1002/2014JD023033>
- Stolz, D. C., Rutledge, S. A., Pierce, J. R., & van den Heever, S. C. (2017). A global lightning parameterization based on statistical relationships among environmental factors, aerosols, and convective clouds in the TRMM climatology. *Journal of Geophysical Research: Atmospheres*, 122, 7461–7492. <https://doi.org/10.1002/2016JD026220>
- Storer, R. L., Van Den Heever, S. C., & Stephens, G. L. (2010). Modeling aerosol impacts on convective storms in different environments. *Journal of the Atmospheric Sciences*, 67(12), 3904–3915. <https://doi.org/10.1175/2010JAS3363.1>
- Tao, W. K., Di Wu, T. M., Peters-Lidard, C., Lang, S., Hou, A., Rienecker, M., et al. (2013). Precipitation intensity and variation during MC3E: A numerical modeling study. *Journal of Geophysical Research: Atmospheres*, 118, 7199–7218. <https://doi.org/10.1002/jgrd.50410>
- Tao, W. K., & Li, X. (2016). The relationship between latent heating, vertical velocity, and precipitation processes: The impact of aerosols on precipitation in organized deep convective systems. *Journal of Geophysical Research: Atmospheres*, 121, 6299–6320. <https://doi.org/10.1002/2015JD024267>
- Tao, W. K., Li, X., Khain, A., Matsui, T., Lang, S., & Simpson, J. (2007). Role of atmospheric aerosol concentration on deep convective precipitation: Cloud-resolving model simulations. *Journal of Geophysical Research*, 112, D24S18. <https://doi.org/10.1029/2007JD008728>
- Tao, W. K., Wu, D., Lang, S., Chern, J. D., Peters-Lidard, C., Fridlind, A., & Matsui, T. (2016). High-resolution NU-WRF simulations of a deep convective-precipitation system during MC3E: Further improvements and comparisons between Goddard microphysics schemes and observations. *Journal of Geophysical Research: Atmospheres*, 121, 1278–1305. <https://doi.org/10.1002/2015JD023986>
- Tewari, M., Chen, F., Wang, W., Dudhia, J., LeMone, M. A., Mitchell, K., et al. (2004). Implementation and verification of the unified Noah land surface model in the WRF model. In *20th conference on weather analysis and forecasting/16th conference on numerical weather prediction*. Seattle, WA: Amer. Meteor. Soc. <https://ams.confex.com/ams/pdfpapers/69061.pdf>
- Thompson, G., & Eidhammer, T. (2014). A Study of Aerosol Impacts on Clouds and Precipitation Development in a Large Winter Cyclone. *Journal of the Atmospheric Sciences*, 71(10), 3636–3658. <https://doi.org/10.1175/jas-d-13-0305.1>
- Van den Heever, S. C., Carrió, G. G., Cotton, W. R., DeMott, P. J., & Prenni, A. J. (2006). Impacts of nucleating aerosol on Florida storms Part I: Mesoscale simulations. *Journal of the Atmospheric Sciences*, 63, 1752–1775. <https://doi.org/10.1175/jas3713.1>
- Varble, A., Fridlind, A. M., Zipser, E. J., Ackerman, A. S., Chaboureaud, J.-P., Fan, J., et al. (2011). Evaluation of cloud-resolving model intercomparison simulations using TWP-ICE observations: Precipitation and cloud structure. *Journal of Geophysical Research*, 116, D16203. <https://doi.org/10.1029/2010JD015180>
- Varble, A., Zipser, E. J., Fridlind, A. M., Zhu, P., Ackerman, A. S., Chaboureaud, J.-P., et al. (2014a). Evaluation of cloud-resolving and limited area model intercomparison simulations using TWP-ICE observations: 1 Deep convective updraft properties. *Journal of Geophysical Research: Atmospheres*, 119, 13,891–13,918. <https://doi.org/10.1002/2013JD021371>
- Varble, A., Zipser, E. J., Fridlind, A. M., Zhu, P., Ackerman, A. S., Chaboureaud, J.-P., et al. (2014b). Evaluation of cloud-resolving and limited area model intercomparison simulations using TWP-ICE observations: 2. Precipitation microphysics. *Journal of Geophysical Research: Atmospheres*, 119, 13,919–13,945. <https://doi.org/10.1002/2013JD021372>
- Wang, C. (2005). A modeling study of the Response of Tropical Deep Convection to the Increase of Cloud Condensation Nuclei Concentration: 1 Dynamics and microphysics. *Journal of Geophysical Research*, 110, D21211. <https://doi.org/10.1029/2004JD005720>
- Weisman, M. L., & Klemp, J. B. (1982). The dependence of numerically simulated convective storms on vertical wind shear and buoyancy. *Monthly Weather Review*, 110(6), 504–520. [https://doi.org/10.1175/1520-0493\(1982\)110<0504:TDOJNSC>2.0.CO;2](https://doi.org/10.1175/1520-0493(1982)110<0504:TDOJNSC>2.0.CO;2)
- Weisman, M. L., & Klemp, J. B. (1984). The structure and classification of numerically simulated convective storms in directionally varying wind shears. *Monthly Weather Review*, 112(12), 2479–2498. [https://doi.org/10.1175/1520-0493\(1984\)112<2479:TSAACON>2.0.CO;2](https://doi.org/10.1175/1520-0493(1984)112<2479:TSAACON>2.0.CO;2)
- Xu, K.-M., & Randall, D. A. (2001). Updraft and downdraft statistics of simulated tropical and midlatitude cumulus convection. *Journal of the Atmospheric Sciences*, 58(13), 1630–1649. [https://doi.org/10.1175/1520-0469\(2001\)058<1630:UADSOS>2.0.CO;2](https://doi.org/10.1175/1520-0469(2001)058<1630:UADSOS>2.0.CO;2)
- Xu, W., & Zipser, E. J. (2012). Properties of deep convection in tropical continental, monsoon, and oceanic rainfall regimes. *Geophysical Research Letters*, 39, L07802. <https://doi.org/10.1029/2012GL051242>
- Zhu, P., Dudhia, J., Field, P. R., Wapler, K., Fridlind, A., Varble, A., et al. (2012). A limited area model (LAM) intercomparison study of a TWP-ICE active monsoon mesoscale convective event. *Journal of Geophysical Research*, 117, D11208. <https://doi.org/10.1029/2011JD016447>
- Zipser, E. J., & Lutz, K. R. (1994). The vertical profile of radar reflectivity of convective cells: A strong indicator of storm intensity and lightning probability? *Monthly Weather Review*, 122(8), 1751–1759. [https://doi.org/10.1175/1520-0493\(1994\)122<1751:TVPORR>2.0.CO;2](https://doi.org/10.1175/1520-0493(1994)122<1751:TVPORR>2.0.CO;2)